A stable microtubule bundle formed through an orchestrated multistep process controls quiescence exit

Damien Laporte[1]*, Aurélie Massoni-Laporte[1], Charles Lefranc[1], Jim Dompierre[1], David Mauboules[1], Emmanuel. T. Nsamba[2], Anne Royou[1], Lihi Gal[3], Maya Schuldiner[3], Mohan L. Gupta Jr[2], Isabelle Sagot[1]

Affiliation :

1: Univ. Bordeaux, CNRS, IBGC, UMR 5095, Bordeaux, France

2: Genetics, Development, and Cell Biology, Iowa State University, Ames, IA 50011, USA.

3: Department of Molecular Genetics, Weizmann Institute of Science, Rehovot, Israel

* Corresponding author: Damien.laporte@ibgc.cnrs.fr

Abstract

Cells fine-tune microtubule assembly in both space and time, to give rise to distinct edifices with specific cellular functions. In proliferating cells, microtubules are highly dynamics, yet, proliferation cessation often lead to their stabilization. One of the most stable microtubule structures identified to date is the nuclear bundle assembled in yeast quiescent cells. In this report, we characterize the original multistep process driving the assembly of this structure in an AuroraB/Ipl1-dependent mechanism. This process follows a precise temporality that relies on the sequential actions of kinesin-14, kinesins-5 and involves both microtubule-kinetochore and kinetochore-kinetochore interactions. Upon quiescence exit, the microtubule bundle disassembles via a cooperative process involving the Kinesin-8 and its full disassembly is required to authorize cells re-entry into proliferation. Overall, our study not only provides the first description, at the molecular scale, of the entire life cycle of a stable microtubule structure *in vivo*, but also sheds light on its function as a sort of "checkpoint" for cell cycle resumption.

35 **Introduction**

36 Microtubules (MT) are hollow cylindrical polymers assembled by the non-covalent
37 interaction of α- and β-tubulin heterodimers. MTs are generally nucleated at MT organizing
38 centers (MTOC) by a ɣ-tubulin complex (ɣ-TuC) that acts as a template and stabilizes the so-
39 called MT "minus-end" (Liu et al., 2021; Roostalu and Surrey, 2017; Sanchez and Feldman,
40 2017; Thawani and Petry, 2021). At the opposite end, the "plus-end" (+end), MTs elongate
41 by the addition of GTP tubulin. The β-tubulin bound GTP is hydrolyzed and stable but
42 transient GDP + Pi intermediates are generated in the region immediately trailing the
43 growing +end. A subsequent Pi release favors MT depolymerization that can be rescued by
44 *de novo* GTP-tubulin addition (Cleary and Hancock, 2021; Gudimchuk and McIntosh, 2021).
45 As such, MTs alternate periods of growth and shrinkage, a behavior called dynamic
46 instability (Mitchison and Kirschner, 1984). *In vivo*, a profusion of MT associated proteins
47 (MAPs) regulate MT length and dynamics (Bodakuntla et al., 2019; Goodson and Jonasson,
48 2018). Besides, MTs are often assembled from multiple tubulin variants or isotypes, and
49 modified by a cohort of post-translational modifications that modulate MT dynamics directly
50 or by influencing the recruitment of MAPs (Janke and Magiera, 2020; Roll-Mecak, 2020).
51 Other MAPs organize MTs into high-ordered edifices either by cross-linking MTs or by
52 connecting them with cellular structures such as membranes, chromosomes or components
53 of the actin cytoskeleton (Bodakuntla et al., 2019; Meiring et al., 2020). Cells fine-tune these
54 mechanisms both in space and in time to give rise to distinct MT architectures with specific
55 function.

56 In proliferating cells, MT dynamic is crucial for their functions. It allows exploring the
57 cell volume searching for structures to "capture", like centromeres during mitosis, or to
58 exert pushing or pulling forces required for various cellular processes such as cell migration

59 or morphogenesis (Heald and Khodjakov, 2015; Kirschner and Mitchison, 1986). Yet, the MT
60 cytoskeleton can extensively rearrange and assemble more stable MT structures, notably
61 when cells change fate (Meiring et al., 2020; Röper, 2020). For example, in terminally-
62 differentiated cells, such as epithelial cells, cardiomyocytes or neurons, stable MT networks
63 make up the majority, and ensure critical cellular functions such as cell shape maintenance
64 or long-distance intra-cellular transport (Baas et al., 2016; Muroyama and Lechler, 2017).
65 Defects in MT stabilization are at the origin of many human pathologies, including neuro-
66 degenerative diseases and ciliopathies (Anvarian et al., 2019; Wheway et al., 2018). Effectors
67 responsible for MT stabilization have been actively searched for since the 1980's. In
68 mammals, the involvement of specific MAPs such as Tau, MAP2, MAP6 and PRC1, or tubulin
69 post-translational modifications have been extensively studied. While their contributions to
70 MT stabilization are central and undisputable, their sole actions do not fully explain the
71 observed levels of MT stability in many types of non-dividing cells (Hahn et al., 2019).
72 For years, yeast species have been instrumental in deciphering mechanisms that
73 regulate MT dynamics in eukaryotes. While proliferating yeast cells display a dynamic MT
74 network (Winey and Bloom, 2012), proliferation cessation goes with the formation of
75 dramatically stable MT structures in both *S. cerevisiae* and *S. pombe* (Laporte and Sagot,
76 2014; Laporte et al., 2013, 2015). Upon quiescence establishment, *S. cerevisiae* assemble a
77 bundle composed of stable parallel MTs, hereafter called Q-nMT bundle, for Quiescent-cell
78 nuclear Microtubule bundle, that emanates from the nuclear side of the spindle pole body
79 (SPB), the yeast equivalent of the centrosome. The Q-nMT bundle spans the entire nucleus
80 and relocalizes kinetochores and centromeres that remain attached to its MT +ends (Laporte
81 and Sagot, 2014). Since MTs embedded into the Q-nMT bundle are not all of the same
82 length, they confer to the structure a typical arrow shape. When cells exit quiescence, the Q-

83 nMT bundle depolymerizes and, by pulling the attached centromeres back to the SPB, allows
84 the recovery of the typical Rabl-like configuration of chromosomes found in G1 yeast cells
85 (Jin et al., 1998). The molecular mechanisms underlying the formation of this peculiar stable
86 MT structure and its physiological function(s) are not understood. Yet, cells impaired for Q-
87 nMT bundle formation have a compromised survival rate in quiescence and a drastically
88 reduced fitness upon cell cycle re-entry (Laporte and Sagot, 2014; Laporte et al., 2013,
89 2015).

90 Here, we demonstrate that the Q-nMT bundle formation is a multistep process that
91 follows a precise temporal sequence. The first step requires the kinesin-14 Kar3, its regulator
92 Cik1 and the EB1 homolog Bim1, and leads to the formation of a short (≈ 1 µm) and stable
93 bundle that resembles a half mitotic spindle. Importantly, in this first step, MT
94 polymerization and stabilization are coupled. In a second step, additional MTs polymerize
95 from the SPB, elongate, and are zipped to pre-existing ones in a Cin8/kinesin-5 dependant
96 manner. The full Q-nMT bundle stabilization is established in a third and last step that
97 requires the kinesin-5 Kip1. Our observations further indicate that Q-nMT bundle assembly
98 requires not only MT-kinetochore attachment but also inter-kinetochore interactions.
99 Finally, we show that, upon quiescence exit, the Q-nMT bundle disassembles from its +ends,
100 where each MT depolymerizes in coordination with its neighbors, via the action of the
101 depolymerase Kip3, a member of the kinesin-8 family. A complete Q-nMT bundle
102 disassembly is required to authorize cells re-entry into the proliferation cycle. Overall, this
103 study describes for the first time the entire life cycle of a MT structure from the molecular
104 mechanisms involved in its formation and stabilization to its disassembly and further reveals
105 that this atypical quiescent specific structure acts as a sort of “checkpoint” for cell cycle
106 resumption upon quiescence exit.

107 ## Results

108 **The Q-nMT bundle formation is a three-step process**

109 To investigate whether the Q-nMT bundle was stable by default, *i.e.* intrinsically
110 stable, or assembled as a dynamic structure and then stabilized, we quantified Q-nMT
111 bundle length (Fig. 1A) and thickness (Fig. 1B) upon quiescence establishment following
112 carbon source exhaustion. We found that the Q-nMT bundle assembly was a 3-step process.
113 In an initial phase (phase I), MTs elongated from the SPB to reach ≈0.8 µm. The number of
114 these so-called phase I-MTs was about the same as in a mitotic spindle (see inset of Fig. 1B
115 and Sup. Fig. 1A). Importantly, phase I-MTs are resistant to nocodazole (Noc), a MT poison
116 that causes dynamic MT depolymerization, indicating that their stabilization was
117 concomitant with their polymerization (Fig. 1A-B). In a second phase, that started ≈10h after
118 glucose exhaustion, additional MTs emerged from the SPB (phase II-MTs) and elongated
119 along phase-I MTs, approximatively doubling the thickness of the phase I MT bundle (Fig. 1B
120 and Sup Fig. 1A). At this stage, the tip of the newly elongated MTs were instable (Fig. 1A-B).
121 Full Q-nMT bundle stabilization was reached ≈48h after glucose exhaustion (phase III), as
122 Noc treatment affected neither Q-nMT bundle length nor its thickness (Fig. 1A-B and Sup.
123 Fig. 1B). Another way to shed light on the Q-nMT bundle formation steps was to plot Q-nMT
124 bundle width as a function of length for each individual cells before and after Noc treatment
125 (Fig. 1C).

126 To confirm the above multistep process, we first followed Nuf2-GFP, a protein that
127 localize at the MT +end. In phase I, Nuf2-GFP signal relocates from SPB to the distal part of
128 elongating Q-nMT bundles (Sup. Fig. 1D). In phase II, when cells were treated with Noc, the
129 Nuf2-GFP signal followed depolymerizing MTs (Fig. 1D), testifying for the instability of phase
130 II MTs. By contrast, the Nuf2-GFP signal remained immobile in phase III, when cells have fully

131 stabilized Q-nMT bundles (Fig. 1D). Second, we measured the γ-tubulin (Tub4) signal at the
132 SPB and found that Tub4 started accumulating at the SPB at the onset of phase I to reach a
133 plateau at the end of phase II (Fig. 1E and Sup. Fig. 1E). Interestingly, the amount of Tub4 at
134 the SPB was proportional to the thickness of the Q-nMT bundle (Sup. Fig. 1F). Finally, in
135 order to confirm the two waves of MT elongation, we developed a strain expressing mTQZ-
136 Tub1 from the endogenous TUB1 promoter and mRuby-TUB1 under the ADH2 promoter, a
137 promoter that is active only after glucose exhaustion. We observed that mRuby-TUB1 was
138 incorporated into the Q-nMT bundle only after phase I (Fig. 1F and Sup. Fig. 1G) confirming
139 the existence of a second wave of MT elongation in phase II. All the above information lead
140 us to propose the model presented in Fig. 1G (see figure legend).
141
142 **Q-nMT bundle formation is an active process regulated in time**
143 Increasing viscosity of the cytoplasm was shown to dampen MT dynamics (Molines et
144 al., 2022). Upon quiescence establishment, yeast cells experience a fluid phase to solid-like
145 transition (Munder et al., 2016; Joyner et al., 2016) and an acidification (Jacquel et al., 2021)
146 that could contribute to Q-nMT bundle formation. Several evidences indicate that these
147 changes in physico-chemical properties are not involved in Q-nMT formation. First, 4-day-old
148 quiescent cells can simultaneously display both dynamic cytoplasmic MTs (cMT) and a stable
149 Q-nMT bundle (Sup. Fig. 1H and (Laporte et al., 2013)). Second, when we mimicked a fluid
150 phase to solid like transition in proliferating cells by artificially dropping the pH, no stable
151 MTs were observed, while F-actin aggregation was induced (Sup. Fig. 1I) as expected from
152 (Peters et al., 2013). Third, 2-day-old quiescent cells displaying a phase III Q-nMT bundle
153 were able to grow *de novo* dynamic MTs after a pulsed-chase Noc treatment (Sup. Fig. 1J).

154 If Q-nMT bundle formation was solely depending on physico-chemical changes, this
155 structure should be able to assemble in late quiescence. By treating cells with Noc upon
156 glucose exhaustion, we managed to prevent Q-nMT bundle formation in early quiescence
157 (Fig. 1H). Strikingly, when the drug was washed out 24 h later, no Q-nMT bundle assembled,
158 even several days after Noc removal (Fig. 1H). We verified that these cells did enter
159 quiescence as they assembled actin bodies (Fig. 1H, right panel), another quiescent cell
160 specific structure (Sagot et al., 2006). This experiment strongly suggests that Q-nMT
161 formation is an active process induced by a transient signal emitted upon glucose
162 exhaustion.

163 Mutants that cannot assemble Q-nMT bundle have a reduced viability in quiescence
164 and a decreased capacity to form colonies upon quiescence exit (Laporte et al., 2013). To
165 establish a causal link between the absence of Q-nMT bundle and the above phenotypes, we
166 took advantage of our ability to prevent conditionally Q-nMT bundle formation in WT cells
167 using early Noc treatment. We demonstrated that in the absence of Q-nMT bundle, both
168 prototroph and auxotroph WT cells loose viability in quiescence and that survivors had a
169 reduced capacity to generate a progeny upon quiescence exit (Sup. Fig. 1K). This reinforce
170 the idea that the Q-nMT bundle is required for cell survival upon chronological aging.

171

172 **Tubulin steady state level and Tub3 isoform are critical for Q-nMT bundle formation.**

173 We then focused on deciphering the molecular mechanisms involved in Q-nMT
174 bundle formation. Yeast cells express two α-tubulin isotypes, Tub1 and Tub3. In proliferating
175 cells, Tub1 make up the majority (Aiken et al., 2019; Nsamba et al., 2021; Schatz et al., 1986).
176 In 4-day-old cells, both isoforms were embedded into the Q-nMT bundle (Fig. 2A and Sup.
177 Fig. 2A). As Tub3 stabilizes MTs *in vitro* (Bode et al., 2003), it may be key for Q-nMT bundle

178 formation in quiescence. To test this hypothesis, we first analyzed the phenotype of *tub3Δ*
179 cells. In phase II, *tub3Δ* cells displayed short MT bundles that were highly sensitive to Noc. In
180 phase III, no MT bundle could be detected (Fig. 2B). Thus in this mutant, MT bundles
181 assembled during phase I were not stable and ultimately collapsed. Yet, in *tub3Δ* cells, the
182 steady state amount of α-tubulin is significantly decreased (Sup. Fig. 2B and (Nsamba et al.,
183 2021)). Thus, the amount of α-tubulin, but not Tub3 itself, could be important for Q-nMT
184 bundle formation. Indeed, mutants impaired for α- and β-tubulin folding, such as the
185 prefolding complex mutants *pac10Δ*, *gim3Δ* or *yke2Δ,* or for tubulin heterodimer formation
186 such as *pac2Δ*, or for β-tubulin folding, such as *cin2Δ* or *cin4Δ*, all of which displaying a
187 decreased amount of tubulin, were unable to assemble a Q-nMT bundle (Sup. Fig. 2C-D).
188 To identify the role of Tub3 *per se*, we took advantage of the "*Tub1-only*" mutant in
189 which the *TUB3* gene was replaced by the *TUB1* gene at the *TUB3* locus. This mutant only
190 expresses Tub1 and displays an α-tubulin level similar to WT (Sup. Fig. 2B and (Nsamba et al.,
191 2021)). We found that "*Tub1-only*" cells display shorter but stable Q-nMT bundles in phase
192 III (Fig. 2C). Interestingly, "*Tub1-only*" Q-nMT bundles were thinner than WT Q-nMT bundles
193 (Fig. 2D). Overall, these data indicate Tub3 is involved in MT elongation in phase II.
194
195 **Kinetochores are critical for phase I but dispensable for the maintenance of Q-nMT**
196 **bundles.**
197 Kinetochore components are enriched at the Q-nMT bundle +end ((Laporte et al.,
198 2013) and Sup Fig. 3A). We thus wondered if kinetochore-MT attachment could play a role in
199 Q-nMT bundle formation. First, we disrupted kinetochore-MT attachment upon phase I
200 using the well-established *ndc80-1* allele (Cheeseman et al., 2006; DeLuca et al., 2018; Wigge
201 et al., 1998). As shown in Fig. 3A, no Q-nMT bundles were detected in *ndc80-1* cells shifted

202 to 37°C at the onset of quiescence entry. Second, we focused on the chromosomal
203 passenger complex (CPC: Bir1/Survivin, Sli15/INCENP, Nbl1/Borealin and Ipl1/Aurora B), a
204 complex known to regulate kinetochore-MT attachment dynamics (Cairo and Lacefield,
205 2020). We found that upon quiescence entry, Ipl1 inactivation impeded MT bundle
206 formation (Fig. 3B). While we could not detect Ipl1 and Ndc1 in quiescent cells, we found
207 that Sli15-GFP and Bir1-GFP localized along the Q-nMT bundle with an enrichment at the Q-
208 nMT bundle +end (Fig. 3C). The deletion of Sli15 did not affect Q-nMT bundle (Fig. Sup. 3E).
209 However, in 4-days old *bir1Δ* cells, Q-nMT bundle length were slightly shorter and not fully
210 stabilized (Fig. 3D). Finally, we investigated the involvement of Bim1, a MT +end binding
211 protein that plays a role in kinetochore MT-end on attachment (Dudziak et al., 2021; Thomas
212 et al., 2016). We have previously shown that Bim1 localizes all along the Q-nMT bundle but
213 that its deletion has no impact on Q-nMT bundle formation even in the presence of Noc
214 ((Laporte et al., 2013) and Fig. 3D). Interestingly, the amount of Bim1 was correlated with
215 tubulin incorporation during Q-nMT bundle formation (Sup Fig. 3D). When we combined
216 *bim1Δ* with *bir1Δ,* cells hardly assembled MT structures that vanished after Noc treatment
217 (Fig. 3D). This demonstrates that in the absence of Bim1, Bir1 was critical for Q-nMT bundle
218 stabilization in phase I. A similar phenotype was observed with *SLI15* deletion (Sup Fig. 3E).
219 Interestingly, the viability of *bim1Δ bir1Δ* cells in quiescence was drastically reduced (Sup Fig.
220 3G). Together, these experiments show that kinetochore-MT attachments are critical for the
221 initiation of Q-nMT bundle assembly.

222 We then hypothesized that inter-kinetochore interactions may stabilize the parallel
223 MTs embedded into the Q-nMT bundle. To test this idea, we analyzed MT organization in
224 s*lk19Δ* cells that are defective in kinetochore clustering (Richmond et al., 2013). In
225 quiescence, Slk19 was enriched at both Q-nMT bundle extremities (Fig. 3E). s*lk19Δ* cells

226 displayed shorter and thinner MT structures that were not stable, i.e. sensitive to Noc
227 treatmant (Fig. 3F). Since Bim1 has been involved in kinetochore-kinetochore interaction, we
228 combined s*lk19Δ* with *bim1Δ.* MT structures detected in s*lk19Δ bim1Δ* cells hardly reached
229 ≈1 µm and vanished upon Noc treatment. In addition, kinetochores localized as a rosette
230 around the SPB (Fig. 3F) and cell viability was strongly compromised (Sup. Fig. 3G). This
231 demonstrates that in the absence of Bim1, Slk19 is strictly essential for MT bundling and
232 stabilization in phase I. Furthermore, since kinetochores are known to be cross-linked by the
233 monopolin complex (Mam1, Lrs4, Hrr25 and Csm1 (Corbett et al., 2010)) we analyzed the
234 phenotype of *mam1Δ, lrs4Δ* and *csm1Δ* cells in quiescence. Most of them displayed short MT
235 structures often arranged in a star-like array (Fig. 3G-H, Sup. Fig. 3F). As for Bir1 and Skl19,
236 the combination of *bim1* deletion with monopolin disruption worsens MT structure length
237 and stability (Fig. 3H) and the cell viability was strongly compromised (Sup. Fig. 3G). Cells
238 impaired for Spo13, a protein involved in monopolin recruitment to kinetochores (Lee et al.,
239 2004) displayed a similar phenotype (Fig. 3G-H). Altogether, these experiments show that
240 inter-kinetochore interactions are critical for Q-nMT bundle assembly.

241 Lastly, we investigated if kinetochore-MT interactions were required for Q-nMT
242 bundle stability once it is formed. In 5-days old WT cells, we used a UV-pulsed-laser to break
243 the Q-nMT bundle into two pieces (Fig. 3I). The presence of dynamic cMTs after laser
244 ablation testified for cell viability (Fig. 3I). In most cases, the length of both the released
245 fragment and the fragment attached to the SPB remained constant (Fig. 3I, Sup. Fig. 3H). By
246 contrast, in proliferating cells, dynamic anaphase spindles promptly disassembled following
247 a pulse-laser break (Sup. Fig. 3I). This demonstrates that once Q-nMT bundles are formed,
248 they do not need MT-kinetochore interaction to be maintained. Accordingly, Ndc80 or Ipl1
249 inactivation in cells that are already in quiescence had no effect on the Q-nMT bundle

250 maintenance (Sup. Fig. 3B-C). Importantly, the above experiment indicates that once
251 formed, Q-nMT stability is established and maintained throughout its length.
252
253
254 **Specific kinesins are required for each step of Q-nMT bundle formation**
255 To go further in the deciphering of the molecular mechanism involved in Q-nMT
256 bundle formation, we focused on kinesins. Kar3 is a kinesin that, in complex with its
257 regulator Cik1, can generate parallel MT bundles from a MT organizing center (MTOC) both
258 *in vitro* and in proliferative cells (Manning et al., 1999; Mieck et al., 2015; Molodtsov et al.,
259 2016). In quiescence, we found that Kar3-3GFP localized at the SPB, but also as dots along
260 the Q-nMT bundle (Fig. 4A). In 4 day-old *kar3Δ* cells, the majority of the detected MT
261 structures were extremely short compared to WT (Fig. 4B and Sup Fig. 4A). Same results
262 were obtained in *cik1Δ* but not in *vik1Δ* cells, which lack the alternate Kar3 regulators (Fig.
263 4B). Thus, the Kar3/Cik1 complex is required for phase I.
264 Cin8 is a Kinesin-5 that cross-links MTs (Bodrug et al., 2020; Pandey et al., 2021; Singh
265 et al., 2018), and as such, could play a role in Q-nMT bundle stabilization. Cin8 was hardly
266 detectable in quiescent cells (Sup. Fig. 4B) and *cin8Δ* cells assembled Q-nMT bundles that
267 were thinner than in WT cells (Fig. 4C-E). Yet, these thinner bundles became stabilized in
268 phase III (Fig. 4C and Sup. Fig. 4C-D). Overall, these results strongly suggest that Cin8 is
269 required for phase II MT nucleation and/or elongation but not for stabilization in phase III.
270 Yeast have an additional Kinesin-5 called Kip1 (Fridman et al., 2013). In quiescence,
271 most of the Kip1-GFP signal was observed at the Q-nMT bundle +end (Fig. 4F). In *kip1Δ* cells,
272 phase I was slightly delayed and Q-nMT bundle were not stabilized in phase III (Fig. 4G-H),
273 yet they were as thick as WT Q-nMT bundles (Sup. Fig. 4E). These data demonstrate that

274 Kip1 is required for Q-nMT bundle stabilization in phase III. Of note, in phase I and II, Q-nMT
275 bundles were slightly longer in cells deleted for the Kinesin-8 Kip3, a MT depolymerase
276 ((Fukuda et al., 2014) Fig. 4 G-H and Sup. Fig. 4G) but were unaffected in cells deleted for
277 Kip2, a kinesin that stabilizes cytoplasmic MTs ((Hibbel et al., 2015) Sup. Fig. 4F-G). Taken
278 together our results demonstrate that each phase of Q-nMT bundle assembly involves
279 specific kinesins.
280
281 **Q-nMT bundle disassembly conditions SPB duplication/separation**
282 Finally, we questioned the molecular mechanism of Q-nMT bundle disassembly upon
283 quiescence exit. Cycloheximide prevented Q-nMT bundle disassembly indicating that this
284 process requires *de novo* protein synthesis (Fig. 5A). We then measured Q-nMT bundle
285 thickness upon depolymerization, and found that while Q-nMT bundles shortened, they did
286 not get thinner (Fig. 5B). In agreement, Nuf2-GFP clusters found at the Q-nMT bundle +end
287 moved back to the SPB while the Nuf2-GFP clusters localized in the middle of the structure
288 remained immobile until they are reached by these later (Sup. Fig. 5 A). This shows that all
289 the MT +ends did not start depolymerizing at the same time, and that longer MTs
290 depolymerized first. This finding is in agreement with our model in which MTs are cross-
291 linked all along the Q-nMT bundle length.
292 Since Kip3 is the only well-characterized yeast MT depolymerase, we studied Q-nMT
293 bundle disassembly in *kip3Δ* cells and observed that it was drastically delayed (Fig. 5C), yet
294 its overall depolymerization rate remained unaffected (Sup. Fig. 5B). In fact, we found that in
295 WT cells, Kip3 needs to be resynthesized upon quiescence exit (Fig. 5D). We searched for
296 proteins that could be involved in Q-nMT bundle disassembly together with Kip3. Among
297 proteins required for mitotic spindle disassembly, we found that inactivation of *CDC14*,

298 *CDC15*, *CDH1*, *DCC1* and *TOR1* had no effect on Q-nMT bundle disassembly, just as with the
299 inactivation of Ipl1 or proteins involved in kinetochore-MT attachment (Sup. Fig. 5 C to F).
300 The sole additional actor we found was She1, a dynein regulator (Bergman et al., 2012),
301 which deletion strongly aggravated the *kip3Δ* phenotype (Fig. 5C). Thus, Q-nMT bundle
302 disassembly does not rely on the canonical mitotic spindle disassembly machinery but,
303 rather, specifically required Kip3 and She1.

304 Importantly, when we followed quiescence exit at the individual cell level, Q-nMT
305 bundle depolymerization always preceded SPB duplication/separation (Fig. 5A) and thus, in
306 both WT and in *kip3Δ* cells (Fig. 5E, F). In fact, when we impeded Q-nMT bundle disassembly
307 using *kip3Δ she1Δ*, we found that SPB duplication was severely delayed (Fig. 5G-H, Sup. Fig.
308 5G-H). Importantly, *kip3Δ she1Δ* cells proliferated just like WT cells (Sup. Fig. 5G) and upon
309 quiescence exit, these mutant cells disassembled actin bodies just as in WT cells (Sup. Fig.
310 5I), demonstrating that *kip3Δ she1Δ* cells were not impaired in sensing quiescent exit signals.
311 These observations indicate that Q-nMT bundle has to be disassembled to allow SPB
312 duplication/separation upon quiescence exit and cell cycle re-entry.

313 **Discussion**

314 Our results shed light on the precise temporal sequences that generate a Q-nMT
315 bundle upon quiescence establishment in yeast. From bacteria to human stem cells,
316 modifications of the cell physico-chemical properties are known to accompany quiescence
317 establishment. Among these modifications, a reduction of the cellular volume increases
318 molecular crowding (Joyner et al., 2016) and pH acidification causes changes in the surface
319 charges of macromolecules and viscosity increases (Charruyer and Ghadially, 2018; Jacquel
320 et al., 2021; Munder et al., 2016; Persson et al., 2020). Much evidence points to these
321 modifications as a trigger for the auto-assembly of several types of enzyme-containing
322 granules (Munder et al., 2016; Petrovska et al., 2014; Rabouille and Alberti, 2017), or
323 complex structures such as P-bodies and Proteasome Storage Granules (Peters et al., 2013;
324 Jacquel et al., 2021; Currie et al., 2023). Recently, Molines and colleagues showed that
325 cytoplasmic viscosity modulates MT dynamics *in vivo* (Molines et al., 2022). Here, we show
326 that Q-nMT bundle formation does not rely on modifications of the physicochemical
327 properties that cells experience upon quiescence establishment (Sup. Fig. 1). In fact,
328 dynamic cMTs and a stable Q-nMT bundle can be observed simultaneously in a quiescent
329 cell (Sup. Fig. 1H), while physicochemical properties evolve in parallel both in the nucleus
330 and in the cytoplasm (Joyner et al., 2016). Importantly, reduction of the cellular volume, pH
331 acidification and increased viscosity are observed within minutes upon glucose starvation
332 (Joyner et al., 2016) while the Q-nMT bundle needs a couple of days to be fully assembled
333 (Fig. 1A). Further, we show that its formation cannot be delayed in time (Fig. 1H) and as such
334 probably depends on an active process induced by a transient signal emitted upon glucose
335 exhaustion. We speculate that the SPB may act as a platform that integrates this signal, and
336 transfers it to the MT machinery in order to assemble a stable parallel structure.

337 As it is required for the onset of Q-nMT bundle formation (Fig. 3B), Aurora B/Ilp1, a
338 kinase that plays a key role at the MT-kinetochore interface where it senses tension, could
339 be one of the target of the above-mentioned nutritional signal. In parallel, upon quiescence
340 establishment, chromosomes hyper-condensation (Guidi et al., 2015; Rutledge et al., 2015)
341 may modify tension at the kinetochore/MT interface and as such could contribute to the
342 initiation of phase I. Besides, Bim1 has also been involved in MT-kinetochore attachment
343 (Dudziak et al., 2021; Akhmanova and Steinmetz, 2015). Although it deletion alone has no
344 effect on Q-nMT bundle formation, its role become critical for phase I if kinetochore-MT
345 interaction are already destabilized by the absence of other CPC components such as Sli15
346 and Bir1 (Fig. 3D and Sup. Fig. 3E). Altogether, these observations point to kinetochore-MT
347 interaction as essential for phase I initiation, as confirmed by the absence of Q-nMT bundle
348 in the *ndc80-1* mutant (Fig. 3A).

349 In phase I, SPB-anchored MTs elongate and are concomitantly stabilized (Fig. 1 A-C).
350 This step requires the kinesin-14 Kar3 and its regulator Cik1 (Fig. 4B). During mating
351 (Molodtsov et al., 2016), and in early mitosis, when half-spindles form (Kornakov et al.,
352 2020), Kar3/Cik1, together with Bim1, align and cross-link growing MTs along existing ones,
353 thereby promoting the organization of MTs into parallel bundles. Yet, in mitosis, the kinesin-
354 14/EB1 complex promotes MT dynamics (Kornakov et al., 2020). In phase I, whether the
355 robust MT stabilization depends on the modification of the kinesin-14/EB1 complex
356 properties or is due to additional specific cross-linker(s) remains to be clarified (Fig. 6b).

357 In quiescence, deletion of either monopolin or Slk19 leads to the formation of short,
358 shattered and flared MT structures, phenotypes that are worsened by the deletion of Bim1
359 (Fig. 3F-H and Sup. Fig. 3F). Since Monopolin and Slk19 are involved in kinetochore clustering
360 (Plowman et al., 2019; Rabitsch et al., 2003; Tóth et al., 2000; Lee et al., 2004; Mittal et al.,

361 2019; Movshovich et al., 2008; Richmond et al., 2013; Zeng et al., 1999), we speculate that
362 kinetochore-kinetochore interaction may not only help preventing depolymerization of
363 single MT, but also constrain elongating phase I MTs and facilitate their concomitant cross-
364 linking (Fig. 6c).

365 With the initiation of phase I, Tub4 starts accumulating at the SPB to allow the
366 second wave of MT nucleation observed in phase II. When phase II MTs elongate, they are
367 concurrently stabilized along pre-existing phase I MTs (Fig. 6d). This step relies on the
368 kinesin-5/Cin8 as Q-nMT bundles assembled in *cin8Δ* cells are thinner than WT Q-nMT
369 bundles (Fig. 4C and D). Intriguingly, *in vitro,* the monomeric form of the vertebrate kinesin-5
370 Eg5 promotes MT nucleation and stabilizes lateral tubulin-tubulin contacts (Chen et al 2019).
371 We thus assume that in the absence of Cin8, either nucleation of phase II MTs cannot occur,
372 or phase II MTs can elongate, but cannot be cross-linked and stabilized to phase I MT while
373 they grow, and as such rapidly vanish. An absence of bundle thickening in phase II is also
374 observed in the "*Tub1-only*" mutant *i.e.* in the absence of Tub3. Tubulin isoforms or tubulin
375 PTM can allow the recruitment of specific kinesins and thereby modify MT properties, see
376 for example (Sirajuddin et al., 2014; Peris et al., 2009; Dunn et al., 2008). May Tub3 be
377 important for Cin8 recruitment or function during phase II?

378 Then, MTs elongate, but their distal parts (>1 µm) are not yet stable (Fig. 1A). The
379 full-length Q-nMT bundle stabilization is reached about 2 days after glucose exhaustion. This
380 step depends on the kinesin-5/Kip1 (Fig. 4 G-H and Sup. Fig. 4E) that is essential to cross-link
381 and stabilize elongating MTs during phase III (Fig. 6e). Accordingly, we observed a Kip1
382 enrichment at the Q-nMT bundle +ends (Fig. 4F). Thus, in agreement with their ability to
383 form homo-tetramers able to cross-link (Acar et al., 2013; Kapitein et al., 2005; Scholey et
384 al., 2014; Weinger et al., 2011) and stabilize parallel MTs (Kapitein et al., 2005; Shimamoto

385 et al., 2015; Yukawa et al., 2020), the two yeast kinesin 5 are essential for Q-nMT bundle
386 formation. Yet, in quiescence, just as in mitosis, Kip1 and Cin8 have clearly non-equivalent
387 functions (Roostalu et al., 2011; Shapira and Gheber, 2016).

388 So far, our results indicate that the Q-nMT bundle formation mechanism is different
389 from the one at work during mitotic spindle assembly. Similarly, we show that Q-nMT bundle
390 disassembly relies on a mechanism that does not involves the same pathway than mitotic
391 spindle dismantlement. Indeed, Q-nMT bundle disassembly involves Kip3 (Fig. 5C-D) but is
392 independent of the anaphase-promoting complex and Aurora B (Woodruff et al., 2010).
393 Interestingly, the longest MTs start depolymerizing from their +ends first. Then, when they
394 reach the +ends of shorter MTs, they embark them on depolymerization (Sup. Fig. 5A). This
395 cooperative behavior has been observed *in vitro* within parallel MT bundles (Laan et al.,
396 2008) and our data indicate that such a comportment can exist *in vivo*. In telophase, the CPC
397 localizes to the end of the two half-spindles in order to participate in mitotic spindle
398 disassembly (Ibarlucea-Benitez et al., 2018). Intriguingly, in quiescence, CPC is poised at the
399 Q-nMT bundle + end (Fig. 3C). May this CPC localization facilitate Q-nMT bundle rapid
400 disassembly once environmental conditions become favorable, thus ensuring quiescence
401 exit efficiency?

402 Finally, in the present study, we show that the Q-nMT bundle is required for WT cells
403 survival in quiescence. While we do not yet know why this structure is important to face
404 chronological age, it is clear that the presence of Q-nMT bundle strongly alters the nuclear
405 organization (Laporte et al., 2013; Laporte and Sagot, 2014; Laporte et al., 2016). As
406 chromatin organization influences gene expression, one hypothesis could be that the
407 presence of Q-nMT bundle is required for expression of genes required for cell survival in
408 quiescence. Another attractive hypothesis could be that the Q-nMT bundle is the yeast

409 analog of the primary cilium of mammalian cells. In fact, these two structures formed upon
410 proliferation cessation, they are both composed of highly stable parallel MTs, their
411 formation involve MT motors, and they are both template from the centriole/SPB. More
412 importantly, we show here that the Q-nMT disassembly is needed to authorize nascent SPB
413 separation upon quiescence exit (Fig. 5). Thus, the Q-nMT bundle disassembly may controls
414 reentry into the proliferation cycle, just as the primary cilium does in ciliated mammalian
415 cells (Goto et al., 2017; Kim and Tsiokas, 2011).

416 ## Materiel and Methods

417 **Yeast strains, plasmids and growth conditions**

418 All the strains used in this study are isogenic to BY4741 (*mat a, leu2Δ0, his3Δ0, ura3Δ0,*
419 *met15Δ0)* or BY4742 (*mat alpha, leu2Δ0, his3Δ0, ura3Δ0, lys2Δ0),* available from GE
420 Healthcare Dharmacon Inc. (UK), except in Fig. 2, in which S288c strains were used (Nsamba
421 et al., 2021). BY strains carrying GFP fusions were obtained from ThermoFisher Scientific
422 (Waltham, MA, USA). Integrative plasmid p*Tub1-mTurquoise2-Tub1*, p*Tub1-wasabi-Tub1*,
423 p*Tub1-mRUBY2-Tub1*, p*Tub1-mEOS2-Tub1* were a generous gift of Wei-Lih Lee (Markus et
424 al., 2015). The strain expressing SPC42-mRFP1 is a generous gift from E. O'Shea (Huh et al.,
425 2003). The strain expressing TUB4-mTQZ is generous gift of S. Jaspersen (Burns et al., 2015).
426 Three copies of eGFP in tandem were integrated at the 3' end of *DAD2*, *TUB3* or *KAR3*
427 endogenous loci respectively. Plasmids for expressing Nup2-RFP (p3695) or Bim1-3xGFP
428 (p4587) from the endogenous locus were described in (Laporte et al., 2013).
429 For Fig. 1F, *pHIS3:mTurquoise2-Tub1+3'UTR::LEU2* was integrated at *TUB1* locus, then a
430 pRS303-*ADH2p-mRuby2-Tub1* was integrated at the *HIS3* locus. To generate this plasmid, the
431 *ADH2* promoter was amplified from yeast genomic DNA flanked with NotI and SpeI
432 restrictions sites and inserted in pRS303. The mRuby2-Tub1+3'UTR, including the 116-
433 nucleotide intron and 618 nucleotides downstream the stop codon was cloned between
434 SpeI/SalI sites.
435 Yeast cells were grown in liquid YPDA medium at 30 °C in flasks as described previously in
436 (Sagot et al., 2006) except for experiments using thermosensitive strains, where cells were
437 first grown at 25 °C then shifted at 37 °C for indicated time before imaging.
438 Experiment in Sup. Fig. 1I was performed as described in (Orij et al., 2009, Peters et al.,
439 2013). In brief, proliferating cells were transfered at an OD_{600nm} of 0.5 in Hepes buffer (25

440 mM Hepes, pH 7.4, 200 mM KCl, 1 mM $CaCl_2$, and 2% dextrose) buffered either at pH 4 or
441 7.5, in the presence of 100 µM CCCP (Sigma-Aldrich). After 150 min 30 °C shaking, cells were
442 imaged (for mTQZ-Tub1) or fixed and stained using Alexa Fluor 568–phalloidin (Invitrogen) as
443 described (Sagot et al., 2006).
444 For live cell imaging, 2 µL of the cell culture were spotted onto a glass slide and immediately
445 imaged at room temperature.
446 For quiescence exit, cells were then incubated 2-3 min in liquid YPD and a 2 µL were spread
447 onto a 2 % agarose microscope pad containing YPD. Individual cells were imaged every hour,
448 up to 6 or 12 h at 21°C. For quiescence exit in presence of cycloheximide (Fig. 5A), cells were
449 pre-incubated 30 min in the presence of the drug prior quiescence exit. Cycloheximide was
450 used at 180 µM (Sigma-Aldrich), Nocodazole was used at 30 µg/mL (7.5 µM) (Sigma-Aldrich).

451 **Fluorescence Microscopy**

452 Cells were observed on a fully-automated Zeiss 200M inverted microscope (Carl Zeiss,
453 Thornwood, NY, USA) equipped with an MS-2000 stage (Applied Scientific Instrumentation,
454 Eugene, OR, USA), a Lambda LS 300 Watt xenon light source (Sutter, Novato, CA, USA), a
455 100X 1.4NA Plan-Apochromat objective, and a 5 position filter turret. For RFP imaging we
456 used a Cy3 filter (Ex: HQ535/50 nm – Em: HQ610/75 nm – BS: Q565 nm lp). For GFP imaging,
457 we used a FITC filter (excitation, HQ487/25 nm; emission, HQ535/40 nm; beam splitter,
458 Q505 nm lp). For mTurquoise imaging we used a DAPI filter (Ex: 360/40 nm – Em: 460/50
459 nm– BS: 400 nm). All the filters are from Chroma Technology Corp. Images were acquired
460 using a CoolSnap HQ camera (Roper Scientific, Tucson, AZ, USA). The microscope, camera,
461 and shutters (Uniblitz, Rochester, NY, USA) were controlled by SlideBook software 5. 0.
462 (Intelligent Imaging Innovations, Denver, CO, USA).

463 For PALM (Fig. 4E) a Nikon Ti-Eclipse equipped with iLas2 TIRF arm, laser diodes (405, 488,
464 532, 561, 642 nm), a 100x 1.49 oil (TIRF) objective connected to a EMCCD Camera
465 Photometrics Evolve was used.
466 Immunofluorescence was done as in (Laporte et al. 2015), using AlexaFluor Phalloidin
467 (Invitrogen).
468 For expansion microscopy (Sup Fig. 2A), spheroplasts were obtained as described in (Laporte
469 et al., 2016). After washes in 10 mg/mL NaBH4 in PEMS for 10 min, spheroplasts were
470 seeded on 12 mm round poly-L-lysine coated coverslips, washed twice for 30 min in 100 µL
471 PEM-BAL (PEM + 1% BSA) and incubated with the primary antibodies (anti-GFP from mouse;
472 Roche, ref. 11814460001, 1/50; anti-alpha-tubulin from rat; YOL1/34, Abcam, ref. Ab6161,
473 1/100) for 1 hour at 37°C. Cells were then washed three times in PEM-BAL and incubated
474 with the secondary antibodies (Goat anti-mouse AlexaFluor®488 1/200 and Donkey anti-rat
475 AlexaFluor®555; A11029 and A21434 respectively, ThermoFisher Scientific, Waltham, MA)
476 for 45 min at 37 °C. Cells were then washed three times with PBS. Cells were processed for
477 Expansion Microscopy as previously described in (Bahri et al., 2021). Spheroplasts were
478 incubated for 10 min in 0.25 % GA in PBS, washed in PBS three times for 5 min, and
479 processed for gelation. A drop of 100 µL of ExM MS (8.625% (wt/wt) SA, 2.5% (wt/wt) AA,
480 0.15 % (wt/wt) BIS, 2 M NaCl in 1× PBS) was placed on the chilled Parafilm, and coverslips
481 were put on the drop with cells facing the solution and incubated for 3 min. Then the
482 coverslips were transferred to a 35 µL of ExM MS supplemented with 0.2 % APS and 0.2 %
483 TEMED, with the initiator (APS) added last. Gelation proceeded for 3 min on ice, and samples
484 were incubated at 37 °C in a humidified chamber in the dark for 1 h. Then coverslips with
485 attached gels were transferred into a six-well plate for incubation in 2 mL of digestion buffer
486 (1× TAE buffer, 0.5% Triton X-100, 0.8 M guanidine hydrochloride, pH ~8.3) supplemented

487 with DAPI (1 µg/mL) for 10-15 min at 37 °C, until the gels detached. Fresh proteinase K at 8
488 units/mL was then added and samples incubated at 37 °C for 30 min. Finally, gels were
489 removed and placed in 10mL petri dishes filled with ddH2O for expansion. Water was
490 exchanged at least twice every 30 min, and incubated in ddH2O overnight at RT. Gels
491 expanded between 4× and 4.2× according to SA purity. Expanded cells were imaged with a
492 UPlanS Apo 100×/1.4 oil immersion objective in an Olympus IX81 microscope (Olympus,
493 Tokyo, Japan). For Structured illumination microscopy (SIM, Fig. 7D), a ZEISS Lattice
494 Lightsheet 7 was used.
495 Laser ablation (Fig. 3I) was performed at room temperature with a 100X oil Plan-Apochromat
496 objective lens (NA 1.4) and an Axio-Observed.Z1 microscope (Carl Zeiss) equipped with a
497 spinning disk confocal (Yokogawa), an EMCCD Evolve camera (Photometrics and Roper
498 Scientific) and 491 nm (100 mW; Cobolt calypso) and 561 nm (100 mW; Cobolt Jive) lasers.
499 Images were acquired with Metamorph software (Roper Scientific). Every 5 to 20 s, a Z-series
500 of 0.4 µm steps were acquired. A 355 nm microchip laser (Teem Photonics) with a 21 kHz
501 repetition rate, 0.8 µJ energy/pulse, 2 kW of peak power and 400 ps pulse width, powered
502 with an iLas2 PULSE system (Roper Scientific) was used between 10 to 40 % power with one
503 pulse of a spot length of 100 points. Breakage was considered as successful if a non-
504 alignment between the two remaining Q-n MT bundle fragments was observed.
505 Z-stacks were deconvolved using the Deconvolution Lab plugin (Fig. 1D; Fig. 3C,E,F Fig. 4A,F).
506 In figures 1F, 4A, B, G, supplemental figure 1H and 3B a faint and fuzzy fluorescence signal is
507 detected in some cell cytoplasm using the GFP filter set. This signal is not GFP but rather due
508 to a non-specific yellow background fluorescence.
509 **Image analysis**

510 Distribution and associated statistics were performed using GraphPad Prism 5 (GraphPad
511 Software, Inc. La Jolla, USA). Unless specified, histograms and scatter dot plots show the
512 mean and the error bars indicate SD. MT length was measured on MAX-projected image
513 using imageJ.
514 For MT fluorescence intensity measurement, a line scan (i1) of 4 pixel width containing both
515 FP signal and background was drawn along MTs on SUM projection image (3-4 Z-plans) using
516 ImageJ. A line of 8 pixels width (at the same location) was drawn in order to calculate the
517 intensity of the surrounding background (i2). The real intensity (ir) was calculated as follow:
518 int=(i1-((i2x8)-(i1x4))/4). Similar approach was conducted to measure Tub4 fluorescence
519 intensity (Fig. 1E) *i.e.* (i1) and (i2) were two boxes, the second including the first one.
520 Intensity was calculated as follow: int=[i1-([(i2xi2$_{surface}$)-(i1xi1$_{surface}$)]/(i2$_{surface}$-
521 i1$_{surface}$))*i1$_{surface}$]. For morphometric Q-nMT bundle property distribution (Fig. 1C and 4B)the
522 mean fluorescence intensity was measured in each individual cell, in a finite area localized
523 adjacent to the SPB (0,4 µm – 3-4 Z stack sum projected) as an estimate of Q-nMT bundle
524 width and plotted as a function of the according measured bundle length.
525 For Nuf2 fluorescence intensity measurement at SPB (Sup. Fig. 1D), GFP and RFP line scan
526 measurements were done on a 3-4 Z-plans sum projection. The "SPB localization zone" was
527 defined as the length ending at the second pixel after the brightest RFP signal of Spc42-RFP.
528 The remaining Q-nMT bundle zone was defined as the "+end zone". The total Nuf2-GFP
529 signal detected along the Q-nMT bundle was set to 100 % (sum projection imaged) allowing
530 to determine the percentage of the signal measured at "SPB localization zone" and at "+end
531 zone"
532 Normalized Q-nMT bundle length (Fig. 3C) was done after line scan intensity measurement.
533 mTQZ-Tub1 intensities slopes were first aligned on their inflexion point. To compare Q-nMT

534 bundle with different lengths, we first sorted Q-nMT bundle <1.8 µm. After an artificial
535 isotropic expansion, we fit all MT structures to length order. Then, corresponding mean
536 intensity of Q-nMT bundle (mTZQ-Tub1) and GFP signal were calculated.
537 To measure the Q-nMT bundle depolymerization (Fig. 5A and E), individual Q-nMT bundle
538 length were measured over time. The first measurement was set at 100 % of the length, and
539 the following percentages calculated accordingly. A fluorescence drop above or equal to 25
540 % defines the inflexion point of the slope, and was used to align the different length
541 measurements. The FWHM (Full Width at Half Maximum) was calculated by measuring
542 fluorescence intensity of a line crossing perpendicularly a Q-nMT bundle, from a sum
543 projection. After fitting intensity level with Gaussian distribution and obtained the standard
544 deviation (σ) value, FWHM was calculated using the equation $2\sqrt{(2\ln 2)}\times\sigma$. In Fig. 5B, FWHM
545 was measured at 0.5 µm of the SPB.

546 **Western blots**

547 Western blots were done as described in (Sagot et al., 2006) using anti-GFP antibodies
548 (Roche); anti-Tat1 antibodies (a generous gift from J-P. Javerzat) and antibody against the
549 budding yeast Act1 or Sac6, generous gifts from B. Goode.

550 **Phenotypical analysis of cells without Q-nMT bundle**

551 WT strains were grown to glucose exhaustion (OD ~6.5), washout with “old YPDA” and
552 pulsed with either DMSO or Nocodazole (30µg/mL) for 24 h. Cells were then washed twice in
553 “old YPDA” before being incubated in the same medium. Dead cell measurement was done
554 using methylene blue staining. The capacity of cells to exit quiescence was scored after cells
555 micro-manipulation (N=4, n>100) as described in (Laporte et al., 2011).

556

557 ## Supplemental data

558 **Supplementary Figure 1** further described the 3 steps of Q-nMT bundle formation. It shows
559 the impact of physico-chemical cell properties on MT stabilization and demonstrate that Q-
560 nMT bundle is required for both cell viability in quiescence and quiescence exit fitness.

561 **Supplementary Figure 2** describes the impact of the alpha tubulin level on Q-nMT bundle
562 assembly.

563 **Supplementary Figure 3** demonstrates that kinetochore-MT interactions are not required
564 for Q-nMT bundle maintenance and that mutants affected for kinetochore-kinetochore
565 interactions have a reduced viability in quiescence.

566 **Supplementary Figure 4** impact of various yeast kinesin deletion on Q-nMT bundle
567 morphometric parameters.

568 **Supplementary Figure 5** Q-nMT bundle disassembly in mutants affected for mitotic spindle
569 dismantlement.

570

Acknowledgments

The authors would like to thank the Bordeaux Imaging center for the help in super-resolution imaging. We also thank Zeiss for their help with SIM. We express our gratitude to E. O'Shea, S. Jaspersen, J-P. Javerzat, Wei-Lih Lee and B. Goode for sharing reagents. We would like to thank J-P. Javerzat for helpful and constructive discussions about our work. DL, AML, JD and IS were supported by a grant from the ANR-21-CE13-0023-01, a Ligue Contre le Cancer Régionale – Dordogne grant #193366 and the CNRS. MG and EN were supported by a National Science Foundation grant number MCB-1846262. AR was supported by the Conseil Régional d'Aquitaine (#20111301010) and the CNRS.

Author Contributions

D. Laporte did all the experiments described in this manuscript, except Fig. 1F, 1H, Fig. 5 G-H and Sup. Fig. 5G to I that were performed by A. Massoni-Laporte, together with all image deconvolution, and Fig. 4E and Sup. Fig. 2A and 3A that were done by J. Dompierre. A. Royou helped for pulse-laser experiments of Fig. 3I and Sup Fig. 3H-I. C. Lefranc did molecular biology and western blots. D. Mauboules performed yeast genetic for Fig. 2. M. L. Gupta Jr and E. T. Nsamba created the Tub1-only mutant (Fig. 2). L. Gal and M. Schuldiner performed high throughput deletion screen. IS and DL designed and supervised the experiments. IS and DL wrote the manuscript.

591 **References**

592 Acar, S., D.B. Carlson, M.S. Budamagunta, V. Yarov-Yarovoy, J.J. Correia, M.R. Niñonuevo, W.
593 Jia, L. Tao, J.A. Leary, J.C. Voss, J.E. Evans, and J.M. Scholey. 2013. The bipolar
594 assembly domain of the mitotic motor kinesin-5. *Nat Commun*. 4:1343.
595 doi:10.1038/ncomms2348.

596 Aiken, J., J.K. Moore, and E.A. Bates. 2019. TUBA1A mutations identified in lissencephaly
597 patients dominantly disrupt neuronal migration and impair dynein activity. *Human*
598 *Molecular Genetics*. 28:1227–1243. doi:10.1093/hmg/ddy416.

599 Akhmanova, A., and M.O. Steinmetz. 2015. Control of microtubule organization and
600 dynamics: two ends in the limelight. *Nature Reviews Molecular Cell Biology*. 16:711–
601 726. doi:10.1038/nrm4084.

602 Anvarian, Z., K. Mykytyn, S. Mukhopadhyay, L.B. Pedersen, and S.T. Christensen. 2019.
603 Cellular signalling by primary cilia in development, organ function and disease. *Nat*
604 *Rev Nephrol*. 15:199–219. doi:10.1038/s41581-019-0116-9.

605 Baas, P.W., A.N. Rao, A.J. Matamoros, and L. Leo. 2016. Stability properties of neuronal
606 microtubules. *Cytoskeleton (Hoboken)*. 73:442–460. doi:10.1002/cm.21286.

607 Bahri, H., J. Buratto, M. Rojo, J.P. Dompierre, B. Salin, C. Blancard, S. Cuvellier, M. Rose, A.
608 Ben Ammar Elgaaied, E. Tetaud, J.-P. di Rago, A. Devin, and S. Duvezin-Caubet. 2021.
609 TMEM70 forms oligomeric scaffolds within mitochondrial cristae promoting in situ
610 assembly of mammalian ATP synthase proton channel. *Biochim Biophys Acta Mol Cell*
611 *Res*. 1868:118942. doi:10.1016/j.bbamcr.2020.118942.

612 Bergman, Z.J., X. Xia, I.A. Amaro, and T.C. Huffaker. 2012. Constitutive dynein activity in She1
613 mutants reveals differences in microtubule attachment at the yeast spindle pole
614 body. *Mol Biol Cell*. 23:2319–2326. doi:10.1091/mbc.E12-03-0223.

615 Bodakuntla, S., A.S. Jijumon, C. Villablanca, C. Gonzalez-Billault, and C. Janke. 2019.
616 Microtubule-Associated Proteins: Structuring the Cytoskeleton. *Trends Cell Biol*.
617 29:804–819. doi:10.1016/j.tcb.2019.07.004.

618 Bode, C.J., M.L. Gupta, K.A. Suprenant, and R.H. Himes. 2003. The two alpha-tubulin isotypes
619 in budding yeast have opposing effects on microtubule dynamics in vitro. *EMBO Rep.*
620 4:94–99. doi:10.1038/sj.embor.embor716.

621 Bodrug, T., E.M. Wilson-Kubalek, S. Nithianantham, A.F. Thompson, A. Alfieri, I. Gaska, J.
622 Major, G. Debs, S. Inagaki, P. Gutierrez, L. Gheber, R.J. McKenney, C.V. Sindelar, R.
623 Milligan, J. Stumpff, S.S. Rosenfeld, S.T. Forth, and J. Al-Bassam. 2020. The kinesin-5
624 tail domain directly modulates the mechanochemical cycle of the motor domain for
625 anti-parallel microtubule sliding. *eLife*. 9:e51131. doi:10.7554/eLife.51131.

626 Burns, S., J.S. Avena, J.R. Unruh, Z. Yu, S.E. Smith, B.D. Slaughter, M. Winey, and S.L.
627 Jaspersen. 2015. Structured illumination with particle averaging reveals novel roles

for yeast centrosome components during duplication. *Elife*. 4. doi:10.7554/eLife.08586.

Cairo, G., and S. Lacefield. 2020. Establishing correct kinetochore-microtubule attachments in mitosis and meiosis. *Essays in Biochemistry*. 64:277–287. doi:10.1042/EBC20190072.

Charruyer, A., and R. Ghadially. 2018. Influence of pH on Skin Stem Cells and Their Differentiation. *Curr Probl Dermatol*. 54:71–78. doi:10.1159/000489520.

Cheeseman, I.M., J.S. Chappie, E.M. Wilson-Kubalek, and A. Desai. 2006. The conserved KMN network constitutes the core microtubule-binding site of the kinetochore. *Cell*. 127:983–997. doi:10.1016/j.cell.2006.09.039.

Chen, G.-Y., J.M. Cleary, A.B. Asenjo, Y. Chen, J.A. Mascaro, D.F.J. Arginteanu, H. Sosa, and W.O. Hancock. 2019. Kinesin-5 Promotes Microtubule Nucleation and Assembly by Stabilizing a Lattice-Competent Conformation of Tubulin. *Curr Biol*. 29:2259-2269.e4. doi:10.1016/j.cub.2019.05.075.

Cleary, J.M., and W.O. Hancock. 2021. Molecular mechanisms underlying microtubule growth dynamics. *Curr Biol*. 31:R560–R573. doi:10.1016/j.cub.2021.02.035.

Corbett, K.D., C.K. Yip, L.-S. Ee, T. Walz, A. Amon, and S.C. Harrison. 2010. The monopolin complex crosslinks kinetochore components to regulate chromosome-microtubule attachments. *Cell*. 142:556–567. doi:10.1016/j.cell.2010.07.017.

Currie, S.L., W. Xing, D. Muhlrad, C.J. Decker, R. Parker, and M.K. Rosen. 2023. Quantitative reconstitution of yeast RNA processing bodies. *Proc Natl Acad Sci U S A*. 120:e2214064120. doi:10.1073/pnas.2214064120.

DeLuca, K.F., A. Meppelink, A.J. Broad, J.E. Mick, O.B. Peersen, S. Pektas, S.M.A. Lens, and J.G. DeLuca. 2018. Aurora A kinase phosphorylates Hec1 to regulate metaphase kinetochore-microtubule dynamics. *J Cell Biol*. 217:163–177. doi:10.1083/jcb.201707160.

Dudziak, A., L. Engelhard, C. Bourque, B.U. Klink, P. Rombaut, N. Kornakov, K. Jänen, F. Herzog, C. Gatsogiannis, and S. Westermann. 2021. Phospho-regulated Bim1/EB1 interactions trigger Dam1c ring assembly at the budding yeast outer kinetochore. *EMBO J*. 40:e108004. doi:10.15252/embj.2021108004.

Dunn, S., E.E. Morrison, T.B. Liverpool, C. Molina-París, R.A. Cross, M.C. Alonso, and M. Peckham. 2008. Differential trafficking of Kif5c on tyrosinated and detyrosinated microtubules in live cells. *J Cell Sci*. 121:1085–1095. doi:10.1242/jcs.026492.

Fridman, V., A. Gerson-Gurwitz, O. Shapira, N. Movshovich, S. Lakämper, C.F. Schmidt, and L. Gheber. 2013. Kinesin-5 Kip1 is a bi-directional motor that stabilizes microtubules and tracks their plus-ends in vivo. *J Cell Sci*. 126:4147–4159. doi:10.1242/jcs.125153.

664 Fukuda, Y., A. Luchniak, E.R. Murphy, and M.L. Gupta. 2014. Spatial control of microtubule
665 length and lifetime by opposing stabilizing and destabilizing functions of Kinesin-8.
666 *Curr Biol*. 24:1826–1835. doi:10.1016/j.cub.2014.06.069.

667 Goodson, H.V., and E.M. Jonasson. 2018. Microtubules and Microtubule-Associated Proteins.
668 *Cold Spring Harb Perspect Biol*. 10:a022608. doi:10.1101/cshperspect.a022608.

669 Goto, H., H. Inaba, and M. Inagaki. 2017. Mechanisms of ciliogenesis suppression in dividing
670 cells. *Cell Mol Life Sci*. 74:881–890. doi:10.1007/s00018-016-2369-9.

671 Gudimchuk, N.B., and J.R. McIntosh. 2021. Regulation of microtubule dynamics, mechanics
672 and function through the growing tip. *Nat Rev Mol Cell Biol*. 22:777–795.
673 doi:10.1038/s41580-021-00399-x.

674 Guidi, M., M. Ruault, M. Marbouty, I. Loïodice, A. Cournac, C. Billaudeau, A. Hocher, J.
675 Mozziconacci, R. Koszul, and A. Taddei. 2015. Spatial reorganization of telomeres in
676 long-lived quiescent cells. *Genome Biol.* 16:206. doi:10.1186/s13059-015-0766-2.

677 Hahn, I., A. Voelzmann, Y.-T. Liew, B. Costa-Gomes, and A. Prokop. 2019. The model of local
678 axon homeostasis - explaining the role and regulation of microtubule bundles in axon
679 maintenance and pathology. *Neural Dev*. 14:11. doi:10.1186/s13064-019-0134-0.

680 Heald, R., and A. Khodjakov. 2015. Thirty years of search and capture: The complex simplicity
681 of mitotic spindle assembly. *J Cell Biol*. 211:1103–1111. doi:10.1083/jcb.201510015.

682 Hibbel, A., A. Bogdanova, M. Mahamdeh, A. Jannasch, M. Storch, E. Schäffer, D. Liakopoulos,
683 and J. Howard. 2015. Kinesin Kip2 enhances microtubule growth in vitro through
684 length-dependent feedback on polymerization and catastrophe. *Elife*. 4:e10542.
685 doi:10.7554/eLife.10542.

686 Huh, W.-K., J.V. Falvo, L.C. Gerke, A.S. Carroll, R.W. Howson, J.S. Weissman, and E.K. O'Shea.
687 2003. Global analysis of protein localization in budding yeast. *Nature*. 425:686–691.
688 doi:10.1038/nature02026.

689 Ibarlucea-Benitez, I., L.S. Ferro, D.G. Drubin, and G. Barnes. 2018. Kinesins relocalize the
690 chromosomal passenger complex to the midzone for spindle disassembly. *J Cell Biol*.
691 217:1687–1700. doi:10.1083/jcb.201708114.

692 Jacquel, B., T. Aspert, D. Laporte, I. Sagot, and G. Charvin. 2021. Monitoring single-cell
693 dynamics of entry into quiescence during an unperturbed life cycle. *Elife*. 10:e73186.
694 doi:10.7554/eLife.73186.

695 Janke, C., and M.M. Magiera. 2020. The tubulin code and its role in controlling microtubule
696 properties and functions. *Nat Rev Mol Cell Biol*. 21:307–326. doi:10.1038/s41580-
697 020-0214-3.

698 Jin, Q., E. Trelles-Sticken, H. Scherthan, and J. Loidl. 1998. Yeast nuclei display prominent
699 centromere clustering that is reduced in nondividing cells and in meiotic prophase. *J.*
700 *Cell Biol.* 141:21–29.

701 Joyner, R.P., J.H. Tang, J. Helenius, E. Dultz, C. Brune, L.J. Holt, S. Huet, D.J. Müller, and K.
702 Weis. 2016. A glucose-starvation response regulates the diffusion of
703 macromolecules. *Elife*. 5. doi:10.7554/eLife.09376.

704 Kapitein, L.C., E.J.G. Peterman, B.H. Kwok, J.H. Kim, T.M. Kapoor, and C.F. Schmidt. 2005. The
705 bipolar mitotic kinesin Eg5 moves on both microtubules that it crosslinks. *Nature*.
706 435:114–118. doi:10.1038/nature03503.

707 Kim, S., and L. Tsiokas. 2011. Cilia and cell cycle re-entry: more than a coincidence. *Cell Cycle*.
708 10:2683–2690. doi:10.4161/cc.10.16.17009.

709 Kirschner, M., and T. Mitchison. 1986. Beyond self-assembly: from microtubules to
710 morphogenesis. *Cell*. 45:329–342.

711 Kornakov, N., B. Möllers, and S. Westermann. 2020. The EB1-Kinesin-14 complex is required
712 for efficient metaphase spindle assembly and kinetochore bi-orientation. *J Cell Biol*.
713 219. doi:10.1083/jcb.202003072.

714 Laan, L., J. Husson, E.L. Munteanu, J.W.J. Kerssemakers, and M. Dogterom. 2008. Force-
715 generation and dynamic instability of microtubule bundles. *Proc Natl Acad Sci U S A*.
716 105:8920–8925. doi:10.1073/pnas.0710311105.

717 Laporte, D., F. Courtout, B. Pinson, J. Dompierre, B. Salin, L. Brocard, and I. Sagot. 2015. A
718 stable microtubule array drives fission yeast polarity reestablishment upon
719 quiescence exit. *J. Cell Biol.* 210:99–113. doi:10.1083/jcb.201502025.

720 Laporte, D., F. Courtout, B. Salin, J. Ceschin, and I. Sagot. 2013. An array of nuclear
721 microtubules reorganizes the budding yeast nucleus during quiescence. *J. Cell Biol.*
722 203:585–594. doi:10.1083/jcb.201306075.

723 Laporte, D., F. Courtout, S. Tollis, and I. Sagot. 2016. Quiescent Saccharomyces cerevisiae
724 forms telomere hyperclusters at the nuclear membrane vicinity through a
725 multifaceted mechanism involving Esc1, the Sir complex, and chromatin
726 condensation. *Mol. Biol. Cell*. 27:1875–1884. doi:10.1091/mbc.E16-01-0069.

727 Laporte, D., and I. Sagot. 2014. Microtubules move the nucleus to quiescence. *Nucleus*.
728 5:113–118. doi:10.4161/nucl.28538.

729 Lee, B.H., B.M. Kiburz, and A. Amon. 2004. Spo13 maintains centromeric cohesion and
730 kinetochore coorientation during meiosis I. *Curr Biol*. 14:2168–2182.
731 doi:10.1016/j.cub.2004.12.033.

732 Liu, P., M. Würtz, E. Zupa, S. Pfeffer, and E. Schiebel. 2021. Microtubule nucleation: The
733 waltz between γ-tubulin ring complex and associated proteins. *Curr Opin Cell Biol*.
734 68:124–131. doi:10.1016/j.ceb.2020.10.004.

735 Manning, B.D., J.G. Barrett, J.A. Wallace, H. Granok, and M. Snyder. 1999. Differential
736 regulation of the Kar3p kinesin-related protein by two associated proteins, Cik1p and
737 Vik1p. *J Cell Biol*. 144:1219–1233. doi:10.1083/jcb.144.6.1219.

738 Markus, S.M., S. Omer, K. Baranowski, and W.-L. Lee. 2015. Improved Plasmids for
739 Fluorescent Protein Tagging of Microtubules in Saccharomyces cerevisiae. *Traffic*.
740 16:773–786. doi:10.1111/tra.12276.

741 Meiring, J.C.M., B.I. Shneyer, and A. Akhmanova. 2020. Generation and regulation of
742 microtubule network asymmetry to drive cell polarity. *Curr Opin Cell Biol*. 62:86–95.
743 doi:10.1016/j.ceb.2019.10.004.

744 Mieck, C., M.I. Molodtsov, K. Drzewicka, B. van der Vaart, G. Litos, G. Schmauss, A. Vaziri,
745 and S. Westermann. 2015. Non-catalytic motor domains enable processive
746 movement and functional diversification of the kinesin-14 Kar3. *eLife*. 4:e04489.
747 doi:10.7554/eLife.04489.

748 Mitchison, T., and M. Kirschner. 1984. Dynamic instability of microtubule growth. *Nature*.
749 312:237–242.

750 Mittal, P., A. Chavan, D. Trakroo, S. Shah, and S.K. Ghosh. 2019. Outer kinetochore protein
751 Dam1 promotes centromere clustering in parallel with Slk19 in budding yeast.
752 *Chromosoma*. 128:133–148. doi:10.1007/s00412-019-00694-9.

753 Molines, A.T., J. Lemière, M. Gazzola, I.E. Steinmark, C.H. Edrington, C.-T. Hsu, P. Real-
754 Calderon, K. Suhling, G. Goshima, L.J. Holt, M. Thery, G.J. Brouhard, and F. Chang.
755 2022. Physical properties of the cytoplasm modulate the rates of microtubule
756 polymerization and depolymerization. *Developmental Cell*. 57:466-479.e6.
757 doi:10.1016/j.devcel.2022.02.001.

758 Molodtsov, M.I., C. Mieck, J. Dobbelaere, A. Dammermann, S. Westermann, and A. Vaziri.
759 2016. A Force-Induced Directional Switch of a Molecular Motor Enables Parallel
760 Microtubule Bundle Formation. *Cell*. 167:539-552.e14.
761 doi:10.1016/j.cell.2016.09.029.

762 Movshovich, N., V. Fridman, A. Gerson-Gurwitz, I. Shumacher, I. Gertsberg, A. Fich, M.A.
763 Hoyt, B. Katz, and L. Gheber. 2008. Slk19-dependent mid-anaphase pause in kinesin-
764 5-mutated cells. *J Cell Sci*. 121:2529–2539. doi:10.1242/jcs.022996.

765 Munder, M.C., D. Midtvedt, T. Franzmann, E. Nüske, O. Otto, M. Herbig, E. Ulbricht, P.
766 Müller, A. Taubenberger, S. Maharana, L. Malinovska, D. Richter, J. Guck, V.
767 Zaburdaev, and S. Alberti. 2016. A pH-driven transition of the cytoplasm from a fluid-
768 to a solid-like state promotes entry into dormancy. *eLife*. 5:e09347.
769 doi:10.7554/eLife.09347.

770 Muroyama, A., and T. Lechler. 2017. Microtubule organization, dynamics and functions in
771 differentiated cells. *Development*. 144:3012–3021. doi:10.1242/dev.153171.

772 Nsamba, E.T., A. Bera, M. Costanzo, C. Boone, and M.L. Gupta Jr. 2021. Tubulin isotypes
773 optimize distinct spindle positioning mechanisms during yeast mitosis. *Journal of Cell*
774 *Biology*. 220:e202010155. doi:10.1083/jcb.202010155.

775 Pandey, H., M. Popov, A. Goldstein-Levitin, and L. Gheber. 2021. Mechanisms by Which
776 Kinesin-5 Motors Perform Their Multiple Intracellular Functions. *Int J Mol Sci*.
777 22:6420. doi:10.3390/ijms22126420.

778 Peris, L., M. Wagenbach, L. Lafanechère, J. Brocard, A.T. Moore, F. Kozielski, D. Job, L.
779 Wordeman, and A. Andrieux. 2009. Motor-dependent microtubule disassembly
780 driven by tubulin tyrosination. *J Cell Biol*. 185:1159–1166.
781 doi:10.1083/jcb.200902142.

782 Persson, L.B., V.S. Ambati, and O. Brandman. 2020. Cellular Control of Viscosity Counters
783 Changes in Temperature and Energy Availability. *Cell*. 183:1572-1585.e16.
784 doi:10.1016/j.cell.2020.10.017.

785 Peters, L.Z., R. Hazan, M. Breker, M. Schuldiner, and S. Ben-Aroya. 2013. Formation and
786 dissociation of proteasome storage granules are regulated by cytosolic pH. *J. Cell Biol.*
787 201:663–671. doi:10.1083/jcb.201211146.

788 Petrovska, I., E. Nüske, M.C. Munder, G. Kulasegaran, L. Malinovska, S. Kroschwald, D.
789 Richter, K. Fahmy, K. Gibson, J.-M. Verbavatz, and S. Alberti. 2014. Filament
790 formation by metabolic enzymes is a specific adaptation to an advanced state of
791 cellular starvation. *Elife*. doi:10.7554/eLife.02409.

792 Plowman, R., N. Singh, E.C. Tromer, A. Payan, E. Duro, C. Spanos, J. Rappsilber, B. Snel,
793 G.J.P.L. Kops, K.D. Corbett, and A.L. Marston. 2019. The molecular basis of monopolin
794 recruitment to the kinetochore. *Chromosoma*. 128:331–354. doi:10.1007/s00412-
795 019-00700-0.

796 Rabitsch, K.P., M. Petronczki, J.P. Javerzat, S. Genier, B. Chwalla, A. Schleiffer, T.U. Tanaka,
797 and K. Nasmyth. 2003. Kinetochore recruitment of two nucleolar proteins is required
798 for homolog segregation in meiosis I. *Dev Cell*. 4:535–548. doi:10.1016/s1534-
799 5807(03)00086-8.

800 Rabouille, C., and S. Alberti. 2017. Cell adaptation upon stress: the emerging role of
801 membrane-less compartments. *Curr Opin Cell Biol*. 47:34–42.
802 doi:10.1016/j.ceb.2017.02.006.

803 Richmond, D., R. Rizkallah, F. Liang, M.M. Hurt, and Y. Wang. 2013. Slk19 clusters
804 kinetochores and facilitates chromosome bipolar attachment. *Mol Biol Cell*. 24:566–
805 577. doi:10.1091/mbc.E12-07-0552.

806 Roll-Mecak, A. 2020. The Tubulin Code in Microtubule Dynamics and Information Encoding.
807 *Dev Cell*. 54:7–20. doi:10.1016/j.devcel.2020.06.008.

808 Roostalu, J., C. Hentrich, P. Bieling, I.A. Telley, E. Schiebel, and T. Surrey. 2011. Directional
809 Switching of the Kinesin Cin8 Through Motor Coupling. *Science*.
810 doi:10.1126/science.1199945.

811 Roostalu, J., and T. Surrey. 2017. Microtubule nucleation: beyond the template. *Nat. Rev.*
812 *Mol. Cell Biol.* doi:10.1038/nrm.2017.75.

813 Röper, K. 2020. Microtubules enter centre stage for morphogenesis. *Philos Trans R Soc Lond*
814 *B Biol Sci*. 375:20190557. doi:10.1098/rstb.2019.0557.

815 Rutledge, M.T., M. Russo, J.-M. Belton, J. Dekker, and J.R. Broach. 2015. The yeast genome
816 undergoes significant topological reorganization in quiescence. *Nucleic Acids Res.*
817 43:8299–8313. doi:10.1093/nar/gkv723.

818 Sagot, I., B. Pinson, B. Salin, and B. Daignan-Fornier. 2006. Actin bodies in yeast quiescent
819 cells: an immediately available actin reserve? *Mol. Biol. Cell*. 17:4645–4655.
820 doi:10.1091/mbc.E06-04-0282.

821 Sanchez, A.D., and J.L. Feldman. 2017. Microtubule-organizing centers: from the centrosome
822 to non-centrosomal sites. *Curr. Opin. Cell Biol.* 44:93–101.
823 doi:10.1016/j.ceb.2016.09.003.

824 Schatz, P.J., F. Solomon, and D. Botstein. 1986. Genetically essential and nonessential alpha-
825 tubulin genes specify functionally interchangeable proteins. *Mol Cell Biol*. 6:3722–
826 3733. doi:10.1128/mcb.6.11.3722-3733.1986.

827 Scholey, J.E., S. Nithianantham, J.M. Scholey, and J. Al-Bassam. 2014. Structural basis for the
828 assembly of the mitotic motor Kinesin-5 into bipolar tetramers. *Elife*. 3:e02217.
829 doi:10.7554/eLife.02217.

830 Shapira, O., and L. Gheber. 2016. Motile properties of the bi-directional kinesin-5 Cin8 are
831 affected by phosphorylation in its motor domain. *Sci Rep*. 6:25597.
832 doi:10.1038/srep25597.

833 Shimamoto, Y., S. Forth, and T.M. Kapoor. 2015. Measuring Pushing and Braking Forces
834 Generated by Ensembles of Kinesin-5 Crosslinking Two Microtubules. *Dev Cell*.
835 34:669–681. doi:10.1016/j.devcel.2015.08.017.

836 Singh, S.K., H. Pandey, J. Al-Bassam, and L. Gheber. 2018. Bidirectional motility of kinesin-5
837 motor proteins: structural determinants, cumulative functions and physiological
838 roles. *Cell. Mol. Life Sci.* 75:1757–1771. doi:10.1007/s00018-018-2754-7.

839 Sirajuddin, M., L.M. Rice, and R.D. Vale. 2014. Regulation of microtubule motors by tubulin
840 isotypes and post-translational modifications. *Nat Cell Biol*. 16:335–344.
841 doi:10.1038/ncb2920.

842 Thawani, A., and S. Petry. 2021. Molecular insight into how γ-TuRC makes microtubules. *J*
843 *Cell Sci*. 134:jcs245464. doi:10.1242/jcs.245464.

844 Thomas, G.E., K. Bandopadhyay, S. Sutradhar, M.R. Renjith, P. Singh, K.K. Gireesh, S. Simon,
845 B. Badarudeen, H. Gupta, M. Banerjee, R. Paul, J. Mitra, and T.K. Manna. 2016. EB1
846 regulates attachment of Ska1 with microtubules by forming extended structures on
847 the microtubule lattice. *Nat Commun*. 7:11665. doi:10.1038/ncomms11665.

848 Tóth, A., K.P. Rabitsch, M. Gálová, A. Schleiffer, S.B. Buonomo, and K. Nasmyth. 2000.
849 Functional genomics identifies monopolin: a kinetochore protein required for

850 segregation of homologs during meiosis i. *Cell*. 103:1155–1168. doi:10.1016/s0092-
851 8674(00)00217-8.

852 Weinger, J.S., M. Qiu, G. Yang, and T.M. Kapoor. 2011. A nonmotor microtubule binding site
853 in kinesin-5 is required for filament crosslinking and sliding. *Curr Biol*. 21:154–160.
854 doi:10.1016/j.cub.2010.12.038.

855 Wheway, G., L. Nazlamova, and J.T. Hancock. 2018. Signaling through the Primary Cilium.
856 *Frontiers in Cell and Developmental Biology*. 6.

857 Wigge, P.A., O.N. Jensen, S. Holmes, S. Souès, M. Mann, and J.V. Kilmartin. 1998. Analysis of
858 the Saccharomyces spindle pole by matrix-assisted laser desorption/ionization
859 (MALDI) mass spectrometry. *J. Cell Biol.* 141:967–977.

860 Winey, M., and K. Bloom. 2012. Mitotic spindle form and function. *Genetics*. 190:1197–1224.
861 doi:10.1534/genetics.111.128710.

862 Woodruff, J.B., D.G. Drubin, and G. Barnes. 2010. Mitotic spindle disassembly occurs via
863 distinct subprocesses driven by the anaphase-promoting complex, Aurora B kinase,
864 and kinesin-8. *J Cell Biol*. 191:795–808. doi:10.1083/jcb.201006028.

865 Yukawa, M., Y. Teratani, and T. Toda. 2020. How Essential Kinesin-5 Becomes Non-Essential
866 in Fission Yeast: Force Balance and Microtubule Dynamics Matter. *Cells*. 9:E1154.
867 doi:10.3390/cells9051154.

868 Zeng, X., J.A. Kahana, P.A. Silver, M.K. Morphew, J.R. McIntosh, I.T. Fitch, J. Carbon, and W.S.
869 Saunders. 1999. Slk19p is a centromere protein that functions to stabilize mitotic
870 spindles. *J Cell Biol*. 146:415–425. doi:10.1083/jcb.146.2.415.

871

872 **Abbreviations**

873 MT: microtubule

874 SPB: spindle pole body

875 GTP: guanosine triphosphate

876 MTOC: microtubule organizing centers

877 ɣ-TuC: ɣ-tubulin complex

878 MAPs: microtubule associated proteins

879 Q-nMT bundle: quiescence specific nuclear microtubule bundle

880 CPC : chromosome passenger complex

881

882 ## Figure legends

883 **Figure 1: The formation of the Q-nMT bundle is a three-step process.**

884 **(A)** Nuclear MT length in WT cells expressing mTQZ-Tub1, before (grey) or after a 15 min Noc
885 treatment (blue) upon entry into quiescence.

886 **(B)** MT fluorescence intensity was used as a proxy of Q-nMT bundle width in WT cells
887 expressing mTQZ-Tub1*;* thin line: intensity of an individual cell; bold line: mean intensity;
888 n>60 for each phase. Mean intensity measurement for half pre-anaphase mitotic spindles
889 (purple) phase I (green), phase II (orange) or phase III (red) Q-nMT bundle. To help
890 comparison, in each graph, the dash line indicate the mean intensity in half pre-anaphase
891 mitotic spindle. Representative cells are shown (images in pseudo-colors).

892 **(C)** Morphometric Q-nMT bundle property distribution (length and width) in each phase
893 before and after a 15 min Noc treatment in WT cells expressing mTQZ-Tub1.

894 **(D)** Single WT cells expressing mTQZ-Tub1 (red) and Nuf2-GFP (green) in phase II (23h) or
895 phase III (50h) were deposited on an agarose pad containing Noc and imaged. Blue
896 arrowheads: SPB; white arrows: Nuf2-GFP clusters; time is in min after pad deposition**.**

897 **(E)** Tub4-mTQZ fluorescence intensity measured at the SPB upon entry into quiescence.
898 Representative cells are shown (images in pseudo-colors). Bar is 1µm

899 **(F)** WT cells expressing mTQZ-Tub1 (red) under the *TUB1* promoter and mRuby-Tub1 (green)
900 under the *ADH2* promoter. Representative cells at the indicated time after glucose
901 exhaustion and the associated line-scans are show. The graph shows the percentage of cells
902 harboring both mTQZ and mRuby fluorescence along the Q-nMT bundle. Each circle is the
903 percentage obtained for an independent cell culture, n>200).

904 **(G)** Schematic of the Q-nMT bundle formation. During phase I, stable MTs (green) elongate
905 from the SPB (in grey). During phase II, new MTs (orange) elongated from the SPB and are
906 stabilized along the phase I MTs, but stay dynamic when longer than phase I MTs. In the
907 meantime, Tub4 (blue) increases at the SPB (grey). After phase III, all MTs are stable (red).
908 **(H)** Upon glucose exhaustion, WT cells expressing mTQZ-Tub1 (green) and Nuf2-GFP (red)
909 were pulsed treated with Noc (blue) or DMSO (grey) for 24 h. Noc or DMSO were then
910 chased using carbon exhausted medium and cells were imaged. Representative images of
911 cells 2 d after the chase are shown. Right panel: same experiment done in WT prototroph
912 cells and representative images of cells 4 d after the chase are shown. Tubulin (green) was
913 detected by immunofluorescence, actin (red) by phalloidin and DNA (blue) with DAPI. The
914 mean Q-nMT bundle length (±SD) in the population is indicated.
915 In A, C, E an H, each circle corresponds to a single cell. In A, E, F and H mean and SD are
916 shown, and unpaired T-test p-values are indicated; ***: p-value<10^{-5}. In A, D, F and H bar is
917 2µm.
918
919 **Figure 2: Q-nMT bundle formation is influenced by the alpha-tubulin amount and isoform**
920 **(A)** WT cell (4 d) expressing either Tub3-3GFP (green) and mTQZ-Tub1 (red, top panel) or
921 Tub3-RFP (red) and mWasabi-Tub1 (green, bottom panel). Blue arrowheads point to SPB.
922 **(B)** Nuclear MT length in WT and *tub3Δ* cells expressing mTQZ-Tub1, 36 h (phase II, yellow)
923 and 90 h (phase III, red) after glucose exhaustion, treated 15 min (blue) or not (grey) with
924 Noc. Representative images are shown on the right.
925 **(C)** Nuclear MT length in WT and *Tub1-only* cells expressing mTQZ-Tub1, 36 h (phase II,
926 yellow) and 90 h (phase III, red) after glucose exhaustion, treated 15 min or not with Noc.
927 Representative images are shown on top.

928 **(D)** Fluorescence intensity along the Q-nMT bundle in WT (grey) and *Tub1-only* (blue) cells
929 expressing mTQZ-Tub1 grown for 10 h (phase I), 36 h (phase II), and 90 h (phase III). Thin
930 lines indicate individual cells fluorescence intensity and bold lines, the mean intensity.
931 Dashed lines indicate the maximal mean fluorescence intensity measured in phase I.
932 In B and C, each circle corresponds to a single cell. MT mean length, SD, and unpaired T-test
933 p-value are indicated. In all panels, bar is 2µm.
934
935 **Figure 3: Kinetochore-kinetochore interactions are required for Q-nMT bundle formation.**
936 **(A)** Nuclear MT length distribution in WT (grey) and *ndc80-1* (violet) cells expressing mTQZ-
937 Tub1 (green) and Nuf2-GFP (red), shifted to 37 °C upon glucose exhaustion for the indicated
938 time and imaged after a 20 min Noc treatment. Representative cells shifted for 12 h at 37°C
939 are shown.
940 **(B)** WT (grey) and *ipl1-1* cells (pink) expressing mTQZ-Tub1 were shifted upon glucose
941 exhaustion to 37 °C for 48 h, and imaged after a 20 min Noc treatment. Representative cells
942 are shown.
943 **(C)** WT cells (2 d) expressing mTQZ-Tub1 (red) and Bir1-GFP or Sli15-GFP (green) were
944 imaged. Graphs show Bir1-GFP or Sli15-GFP fluorescence intensity along normalized Q-nMT
945 bundles (plain and dash lines: mean and SD respectively).
946 **(D)** Nuclear MT length distribution in cells of the indicated genotype (4 d) expressing mTQZ-
947 Tub1 treated or not with Noc. Representative cells are shown.
948 **(E)** WT cells expressing mTQZ-Tub1 (red) and Slk19-GFP (green) 4 h after glucose exhaustion.
949 Blue arrowhead: SPB.

950 **(F)** Nuclear MT length distribution in cells of the indicated genotype (4 d) expressing mTQZ-
951 Tub1 (green) and Nuf2-GFP (red) were imaged before or after Noc treatment.
952 Representative cells are shown. White arrowheads point to Nuf2 dots.
953 **(G)** Cells of the indicated genotype (4 d) expressing mTQZ-Tub1 (green) and Nup2-RFP (red).
954 **(H)** Nuclear MT length distribution in cells of the indicated genotype (4 d) expressing mTQZ-
955 Tub1 treated or not with Noc. Representative cells are shown.
956 **(I)** Length variation of nuclear MT bundle fragments after laser ablation (pink dash line) in
957 cells expressing mRuby-TUB1 (red) and Dad2-GFP (green). Time is in min. Blue arrowhead:
958 SPB, white arrowhead: cMT.
959 In A, B, D, F, and H, each circle corresponds to a single cell. Mean, SD, and unpaired T-test p-
960 values are indicated (*: p-value <0.05, and ***: p-value <10^{-6}). Bar is 2 µm except in (I) where
961 it is 1 µm.
962
963 **Figure 4: Each phase of Q-nMT formation requires a specific kinesin.**
964 **(A)** Images and corresponding line scans of WT cells (2 d) expressing Kar3-3GFP (green) and
965 mTQZ-Tub1 (red).
966 **(B)** Morphometric Q-nMT bundle properties distribution in 4 d WT (grey), *kar3Δ* (red), *vik1Δ*
967 (blue), *cik1Δ* cells (green) expressing mTQZ-Tub1 after Noc treatment. Blue crosses are SD.
968 Each circle corresponds to an individual Q-nMT bundle. Representative cells are shown.
969 **(C)** Nuclear MT length distribution in WT and *cin8Δ* cells expressing mTQZ-Tub1 treated
970 (dashed boxes) or not (plain boxes) with Noc.
971 **(D)** Fluorescence intensity along Q-nMT bundle in WT and *cin8Δ* cells expressing mTQZ-Tub1
972 7 h and 24 h after glucose exhaustion. Representative cells are shown.

973 **(E)** WT and *cin8Δ* cells expressing mEOS3.2-Tub1 were imaged using PALM (images are in
974 pseudo-colors). Full width at half maximum (FWHM) was measured at the indicated distance
975 from the SPB. Each line in the bottom graph corresponds to a single cell. P-value between
976 WT and *cin8Δ* are indicated (unpaired T-test).
977 **(F)** WT cells (3 d) expressing Kip1-GFP (green) and mTQZ-Tub1 (red). Graphs show
978 fluorescence intensity along normalized Q-nMT bundles (plain and dash lines: mean and SD
979 respectively).
980 **(G-H)** Representative images and nuclear MT length distribution in WT, *kip1Δ* and *kip3Δ* cells
981 expressing mTQZ-Tub1 treated (dashed boxes) or not (plain boxes) with Noc.
982 In C and H, *: p-value <0.05, and ***: p-value $<10^{-6}$ (unpaired T-test). Means and SD are
983 indicated. In A, B, D, E, F and G, bar is 2 µm.
984
985 **Figure 5: Q-nMT bundle disassembly always occurs before SPB separation upon quiescence**
986 **exit.**
987 **(A)** WT cells expressing Spc42-RFP (red) and Nuf2-GFP (green) (5 d) were re-fed on an YPDA
988 microscope pad. Individual Q-nMT bundles were measured in cells treated with CHX (blue,
989 Stu2-GFP) or with DMSO alone (grey, Nuf2-GFP). Each line corresponds to an individual cell.
990 For each cell, time was set to zero at the onset of MT bundle depolymerization (black dashed
991 line).
992 **(B)** Q-nMT bundle length (green) and fluorescence intensity at full width half maximum
993 (FWHM - orange) were measured upon quiescence exit in WT cells (5 d) expressing mTQZ-
994 Tub1. Representative example of shirking Q-nMT bundle is shown on the left.

995 **(C)** Cells of the indicated genotype expressing mTQZ-Tub1 were grown for 4 d, and re-fed. Q-
996 nMT bundle length was measured at the indicated time points, 15 min after a Noc
997 treatment.

998 **(D)** Western blot (GFP antibodies) on total protein extracts from WT cells expressing Kip3-
999 GFP grown for the indicated time. Sac6 was used as a loading control (Sac6 antibodies).

1000 **(E)** WT and *kip3Δ* cells (5 d) expressing Nuf2-GFP were re-fed on an YPDA microscope pad.
1001 Each line corresponds to an individual cell. For each cell, time was set to zero at the onset of
1002 SPB separation.

1003 (**F**) Representative images of *kip3Δ* cells expressing Nuf2-GFP upon quiescence exit. White
1004 arrowheads: Q-nMT bundle extremities.
1005 (**G**) Percentage of cells expressing Spc42-mRFP1 with separated SPB as a function of time
1006 upon quiescence exit.
1007 (**H**) WT and *kip3Δshe1Δ* cells (6 d) expressing Spc42-mRFP1 (red) and mTQZ-Tub1 (green)
1008 were re-fed on a YPDA microscope pad. Percentage of cells with a single or a duplicated SPB
1009 in the presence or absence of Q-nMT bundle were scored. Representative cells are shown.
1010 Right bottom panel: actin (phalloidin staining, red) in *kip3Δ she1Δ* cells (6 d) expressing
1011 mTQZ-Tub1 (green) before and 1 h after quiescence exit.
1012 In F and H, blue arrowheads: SPB. In all panels, bar is 2 µm.
1013

1014 **Figure 6: Model for Q-nMT bundle assembly**

1015 MT-kinetochore interaction and Ilp1 (Aurora B) are required for the onset of phase I. Kar3
1016 (kinesin-14) and its regulator Cik1 are essential to initiate Q-nMT bundle elongation.
1017 Although deletion of *BIM1* (EB1) has no effect, it becomes critical for phase I if kinetochore-

1018 MT interactions are already destabilized by the absence of Chromosome Passenger Complex
1019 components. Kinetochore clustering by the monopolin complex and Slk19 is needed to
1020 maintain MT bundling while phase I MTs elongate. During phase I, Tub4 (γ-Tubulin)
1021 accumulates at the SPB. In phase II, a second wave of MT nucleation and elongation occur.
1022 Phase II MTs are concurrently stabilized along pre-existing phase I MTs, in a Cin8 (kinesin-5)-
1023 dependent manner. Phase I and phase II MTs + end (>1 µm) remain dynamic until the full
1024 length Q-nMT bundle stabilization is reached via the action of Kip1 (kinesin-5), about 2 days
1025 after glucose exhaustion.

1026

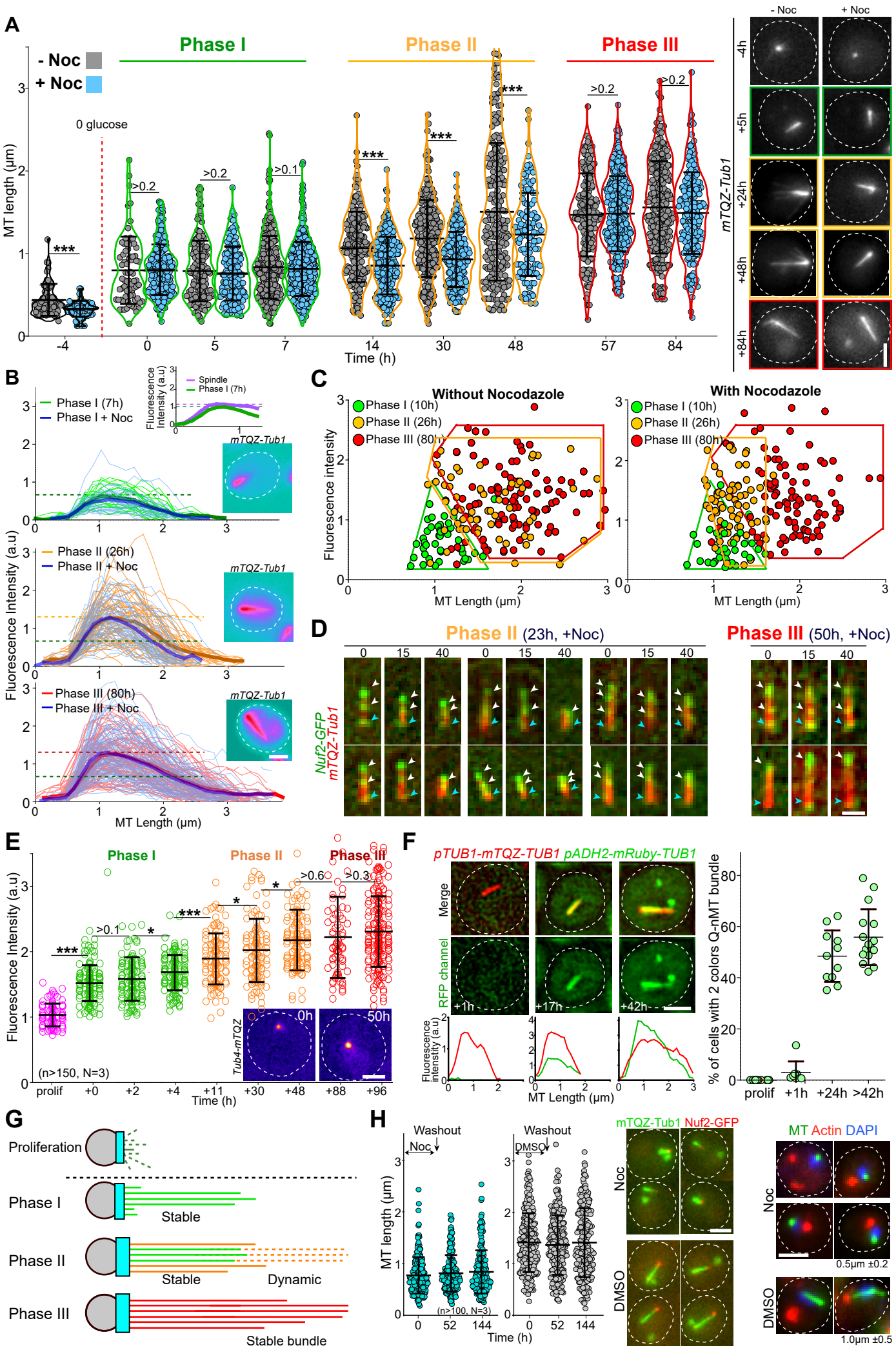
A
Phase I
Phase II
Phase III
- Noc
+ Noc
0 glucose
MT length (µm)
Time (h)
mTQZ-Tub1
B
Phase I (7h)
Phase I + Noc
Phase II (26h)
Phase II + Noc
Phase III (80h)
Phase III + Noc
Fluorescence Intensity (a.u)
MT Length (µm)
Spindle
Phase I (7h)
C
Without Nocodazole
With Nocodazole
Phase I (10h)
Phase II (26h)
Phase III (80h)
Fluorescence intensity
MT Length (µm)
D
Phase II (23h, +Noc)
Phase III (50h, +Noc)
Nuf2-GFP
mTQZ-Tub1
E
Phase I
Phase II
Phase III
Fluorescence Intensity (a.u)
(n>150, N=3)
Tub4-mTQZ
Time (h)
F
pTUB1-mTQZ-TUB1 pADH2-mRuby-TUB1
Merge
RFP channel
MT Length (µm)
% of cells with 2 colors Q-nMT bundle
G
Proliferation
Phase I
Stable
Phase II
Stable
Dynamic
Phase III
Stable bundle
H
Washout
Noc
DMSO
MT length (µm)
(n>100, N=3)
Time (h)
mTQZ-Tub1 Nuf2-GFP
MT Actin DAPI
0.5µm ±0.2
1.0µm ±0.5

Figure 1

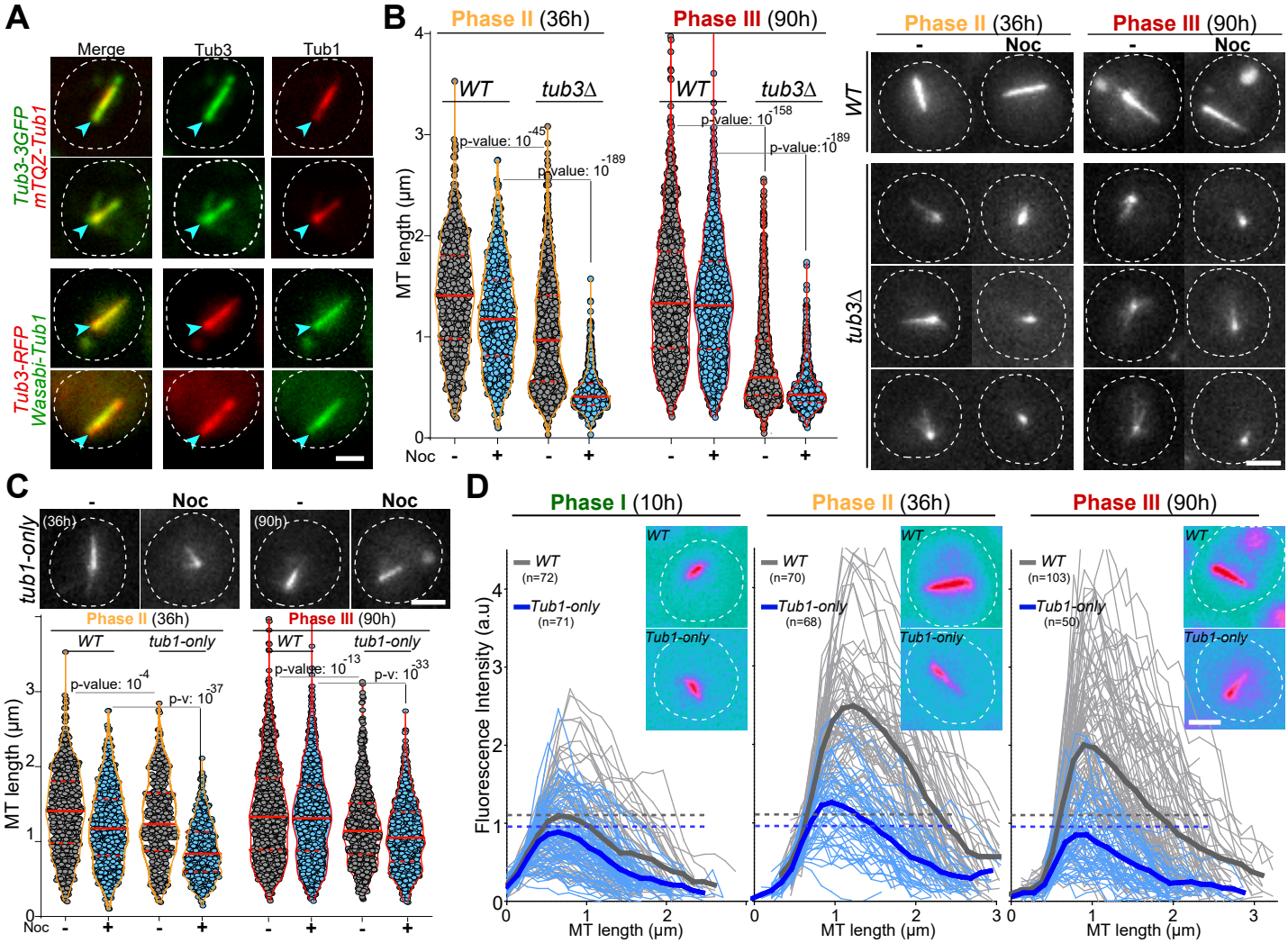
A
Merge
Tub3
Tub1
Tub3-3GFP
mTQZ-Tub1
Tub3-RFP
Wasabi-Tub1
B
Phase II (36h)
Phase III (90h)
WT
tub3Δ
p-value: 10^-45
p-value: 10^-189
p-value: 10^-158
p-value:10^-189
MT length (µm)
Noc
Phase II (36h)
Phase III (90h)
-
Noc
WT
tub3Δ
C
tub1-only
(36h)
(90h)
Phase II (36h)
Phase III (90h)
WT
tub1-only
p-value: 10^-4
p-v: 10^-37
p-value: 10^-13
p-v: 10^-33
MT length (µm)
Noc
D
Phase I (10h)
Phase II (36h)
Phase III (90h)
WT
(n=72)
Tub1-only
(n=71)
(n=70)
(n=68)
(n=103)
(n=50)
Fluorescence Intensity (a.u)
MT length (µm)

Figure 2

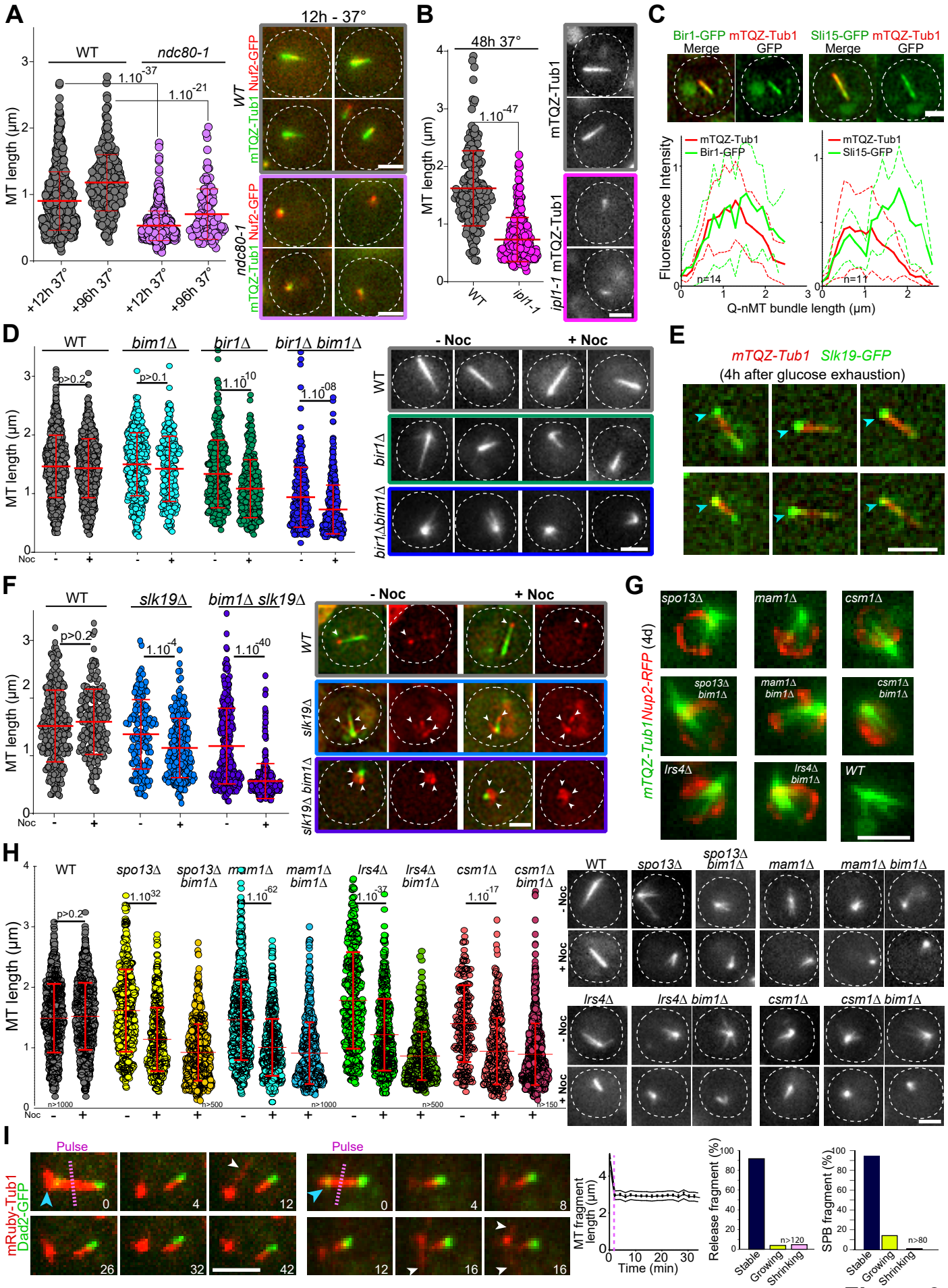
A
12h - 37°
WT
ndc80-1
MT length (µm)
+12h 37°
+96h 37°
mTQZ-Tub1 Nuf2-GFP
B
48h 37°
mTQZ-Tub1
ipl1-1
C
Bir1-GFP mTQZ-Tub1
Sli15-GFP mTQZ-Tub1
Merge
GFP
Fluorescence Intensity
Q-nMT bundle length (µm)
D
bim1Δ
bir1Δ
bir1Δ bim1Δ
- Noc
+ Noc
E
mTQZ-Tub1 Slk19-GFP
(4h after glucose exhaustion)
F
slk19Δ
bim1Δ slk19Δ
G
spo13Δ
mam1Δ
csm1Δ
lrs4Δ
mTQZ-Tub1Nup2-RFP (4d)
H
spo13Δ bim1Δ
mam1Δ bim1Δ
lrs4Δ bim1Δ
csm1Δ bim1Δ
I
Pulse
mRuby-Tub1
Dad2-GFP
MT fragment length (µm)
Time (min)
Release fragment (%)
SPB fragment (%)
Stable
Growing
Shrinking

Figure 3

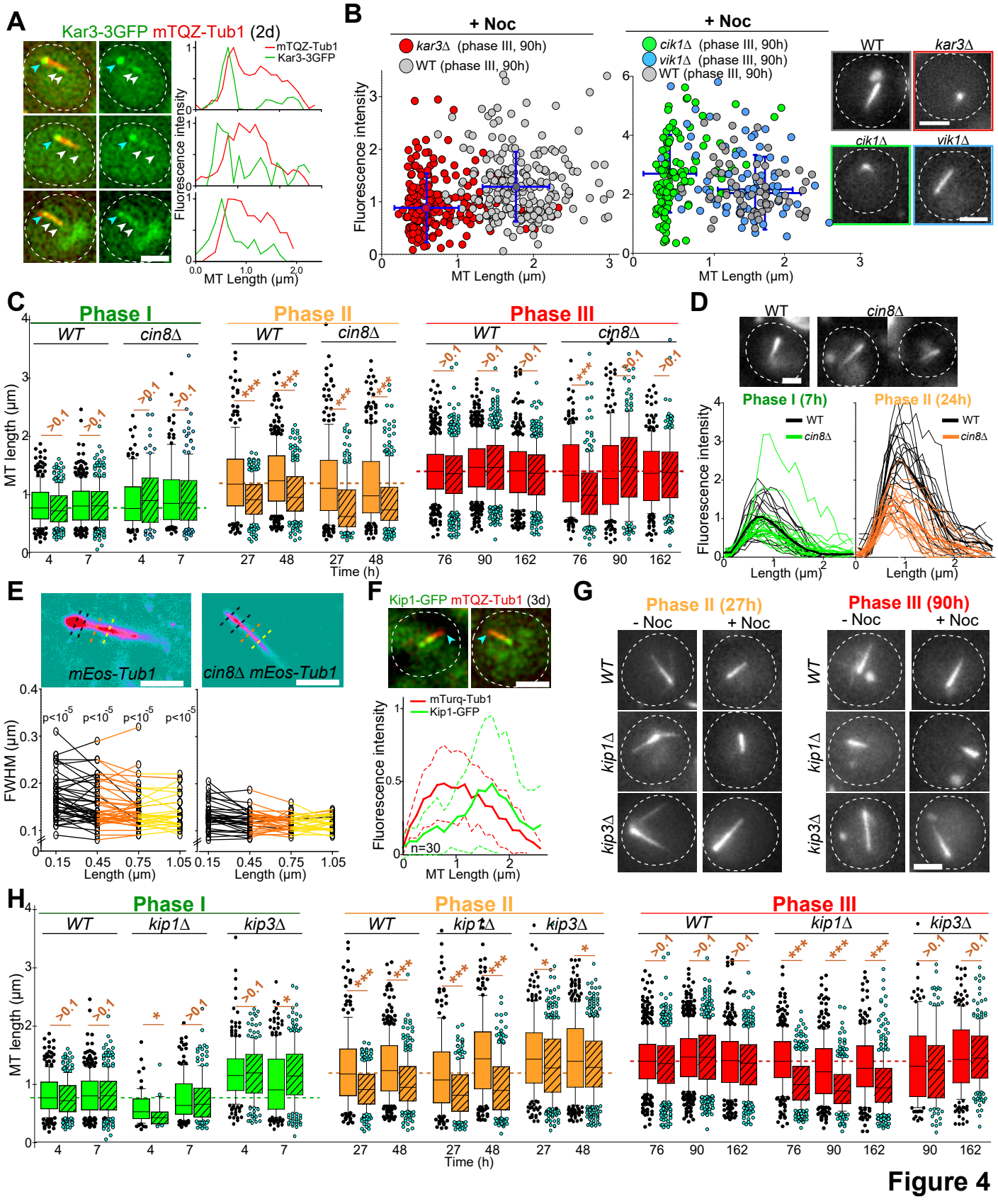
A
Kar3-3GFP mTQZ-Tub1 (2d)
mTQZ-Tub1
Kar3-3GFP
Fluorescence intensity
MT Length (µm)
B
+ Noc
kar3Δ (phase III, 90h)
WT (phase III, 90h)
Fluorescence intensity
MT Length (µm)
+ Noc
cik1Δ (phase III, 90h)
vik1Δ (phase III, 90h)
WT (phase III, 90h)
MT Length (µm)
WT
kar3Δ
cik1Δ
vik1Δ
C
Phase I
Phase II
Phase III
WT
cin8Δ
MT length (µm)
Time (h)
D
WT
cin8Δ
Phase I (7h)
Phase II (24h)
Fluorescence intensity
Length (µm)
E
mEos-Tub1
cin8Δ mEos-Tub1
FWHM (µm)
Length (µm)
F
Kip1-GFP mTQZ-Tub1 (3d)
mTurq-Tub1
Kip1-GFP
Fluorescence intensity
n=30
MT Length (µm)
G
Phase II (27h)
Phase III (90h)
- Noc
+ Noc
WT
kip1Δ
kip3Δ
H
Phase I
Phase II
Phase III
WT
kip1Δ
kip3Δ
MT length (µm)
Time (h)

Figure 4

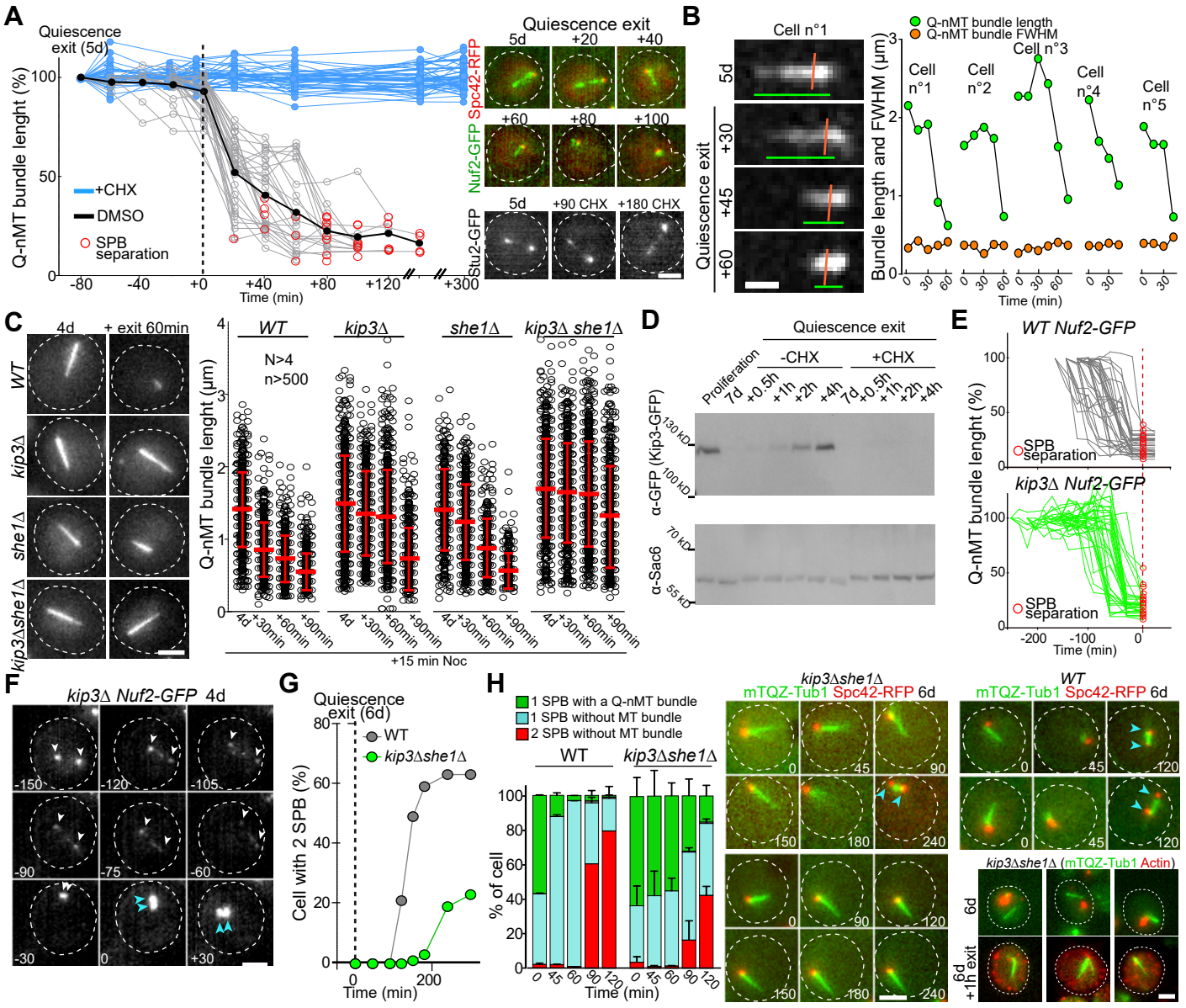
A
Quiescence exit (5d)
Q-nMT bundle lenght (%)
+CHX
DMSO
SPB separation
Time (min)
Quiescence exit
5d
+20
+40
+60
+80
+100
Spc42-RFP
Nuf2-GFP
Stu2-GFP
+90 CHX
+180 CHX
B
Cell n°1
Cell n°2
Cell n°3
Cell n°4
Cell n°5
Q-nMT bundle length
Q-nMT bundle FWHM
Bundle length and FWHM (µm)
Quiescence exit
+30
+45
+60
C
4d
+ exit 60min
WT
kip3Δ
she1Δ
kip3Δshe1Δ
N>4
n>500
Q-nMT bundle lenght (µm)
+15 min Noc
D
Quiescence exit
Proliferation
-CHX
+CHX
α-GFP (Kip3-GFP)
α-Sac6
130 kD
100 kD
70 kD
55 kD
E
WT Nuf2-GFP
kip3Δ Nuf2-GFP
Q-nMT bundle lenght (%)
SPB separation
Time (min)
F
kip3Δ Nuf2-GFP 4d
G
Quiescence exit (6d)
WT
kip3Δshe1Δ
Cell with 2 SPB (%)
Time (min)
H
1 SPB with a Q-nMT bundle
1 SPB without MT bundle
2 SPB without MT bundle
% of cell
kip3Δshe1Δ
mTQZ-Tub1 Spc42-RFP 6d
WT
mTQZ-Tub1 Spc42-RFP 6d
kip3Δshe1Δ (mTQZ-Tub1 Actin)
6d
6d +1h exit

Figure 5

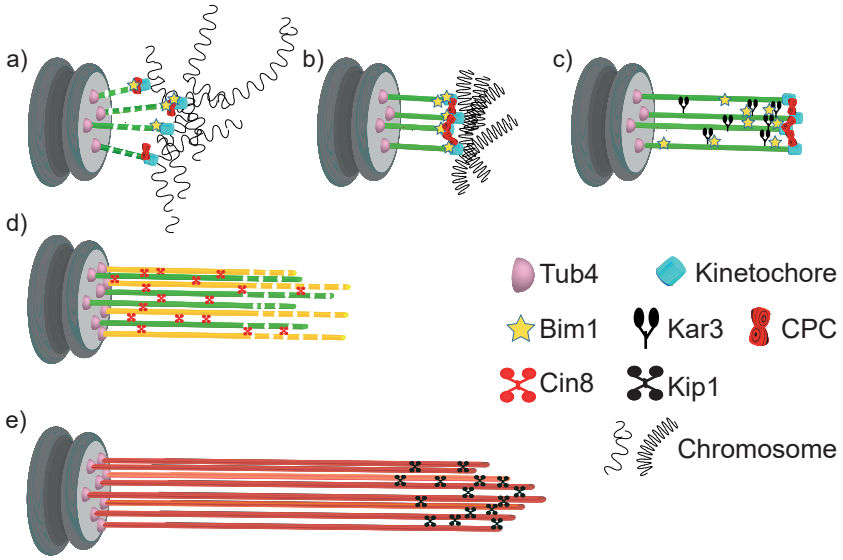

Figure 6